A Fourier transform infrared absorption study of hydrogen and deuterium in hydrothermal ZnO

HANS BJØRGE NORMANN

THESIS SUBMITTED FOR THE DEGREE OF

MASTER OF SCIENCE

IN MATERIALS, ENERGY AND NANOTECHNOLOGY

CENTRE FOR MATERIALS SCIENCE AND NANOTECHNOLOGY
DEPARTMENT OF PHYSICS
UNIVERSITY OF OSLO

DECEMBER, 2008

Acknowledgements

First of all, my sincere thanks go to my supervisor Prof. Bengt Svensson. Your wide knowledge about semiconductors and defects has been a great inspiration and made this research very interesting. I would also thank you for introducing me to the exciting field of transparent conductive oxides and for letting me play with the infrared spectrometer.

Special thanks go to my second supervisor Dr. Leonid Murin for an excellent introduction to FTIR, and for pointing me in the right direction for the many questions I had. Your good sense of humor made the many FTIR lessons a great fun.

I want to thank Viktor Bobal for much needed help when the spectrometer had a total breakdown. Your alignment skills are superior. Without any doubt, your contribution to this work is indispensable. Your help with the ion implantation, wet chemical etch, the TRIM simulation is also highly appreciated.

I would also like to thank my other colleagues at MiNaLab. Dr. Lasse Vines for helping me with the SIMS measurements and the sample polishing. Klaus Magnus Johansen for fruitful discussions, and for showing an interest in my results. Jan Bleka, Hallvard Angelskår, Tariq Maqsood and Lars Løvlie for valuable MatLab and LaTeX-programming. Anders Werner Bredvei Skilbred for help with the SEM, and Øyvind Hanisch for several hilarious non-scientific discussions.

My family Anne, Jånn, Marthe, Tobias, Kirsti and Frode deserve thanks for much needed support and friendship. My very special thanks go to my fiancée Kristin, for endless support in many ways.

Hans Bjørge Normann, Oslo, December 15, 2008

Abstract

As-grown, hydrogen-implanted and deuterium-implanted mono-crystalline hydrothermally grown ZnO samples (cooled to liquid helium temperatures) have been investigated by infrared spectroscopy (FTIR). The hydrogen/deuterium implanted samples were each ion implanted with a total dose of 4×10^{16} cm^{-2}, followed by annealing at 400°C for 70 hours. Several O-H and O-D absorption bands, with excellent isotopic shift, were observed for IR light applied both parallel and perpendicular to the *c* axis of the ZnO crystal.

Combined with a SIMS measurement, the integrated absorbance of the dominating 2644 cm^{-1} O-D mode was used to deduce the absorbance per D species to $\mathcal{E}_{\mathrm{D}} = (1.72 \pm 0.63) \times 10^{-18}$ cm for measurements with the wavevector perpendicular to the *c* axis of the samples. Further, the SIMS results revealed a difference between the concentrations of D and Li of less than a factor two, suggesting that Li is a strong trap for H/D. Finally, the hydrogen content in the as-grown samples is estimated to be $\sim 5 \times 10^{17}$ cm^{-3} based on the absorbance of the prominent 3577 cm^{-1} line.

Contents

Chapter 1

Introduction and goal

Zinc oxide is a widely applied material which has been investigated as an electronic material for many decades. It belongs to the class of transparent conductive oxides (TCO). Fundamental research on ZnO has recently experienced a renaissance, due to the prospective use as an optoelectronic material. Based on the possibility to grow high purity crystals, quantum wells, nanorods and quantum dots, it is hope for obtaining blue and UV optoelectronics, radiation-resistant material for harsh environments, transparent electronic devices, ZnO spintronics, and transparent front electrodes for next generation solar cells [1]. Accomplishing ZnO films with improved electrical and optical properties is one of the key challenges in photovoltaic research and development.

In this thesis we focus on hydrogen impurities in ZnO. Hydrogen has been shown to contribute to *n*-type conductivity and to passivate acceptors, making *p*-doping difficult to attain. The atomic configuration of hydrogen in the crystal structure is still under debate, one experimental technique that can provide detailed information on this issue is vibrational spectroscopy. Hence, we have applied Fourier transform infrared spectroscopy (FTIR) to probe for infrared absorption related to hydrogen bonds in ZnO. The solubility of hydrogen in ZnO is $\sim 10^{15}$ cm^{-3} at RT [2], but even higher concentration can be stable when trapped at impurities. Hence, as-grown ZnO samples could provide hydrogen-related absorption peaks if the hydrogen resides in a IR active configuration, as the concentration is

within the detection limit of FTIR. Further, a known amount of hydrogen and deuterium is subsequently introduced by ion implantation into the samples, and we search for changes in the absorption bands and try to identify isotopic shifts. This could give detailed information of how hydrogen is configured in the crystal structure, and even be used as a non-destructive method for quantitative determination of the hydrogen content in virgin hydrothermally grown ZnO.

1.1 Goal

The objective of this thesis is to study the presence and atomic configuration of hydrogen in mono-crystalline hydrothermally grown ZnO by FTIR. The ultimate goal is to master and understand the hydrogen-related optical properties in the mid-infrared region.

Chapter 2

Background

2.1 Zinc Oxide - ZnO

Crystalline ZnO is naturally occurring as the oxidic mineral zincite. Bragg determined the crystal structure by X-ray diffraction in 1914 [3]. It crystallizes in the hexagonal wurtzite structure with the space group $P6_3mc$[1]. Figure 2.1 and 2.2 show a perspective view of the crystal structure perpendicular and along the c axis, respectively. In principle the Miller-Bravais (0001) plane is terminated by Zn atoms, and the $(000\bar{1})$ is terminated by O atoms only. These surfaces are called the basal planes. A second set of important planes are the non-polar $(10\bar{1}0)$ and $(11\bar{2}0)$ prism planes, which contain the same number of zinc and oxygen atoms. The hexagonal unit cell has dimensions $a = 3.25$ Å and $c = 5.207$ Å. The ratio, $c/a = 1.60$, is approximately that of the ideal close packed wurtzite structure (1.633). Every zinc atom is surrounded by four oxygen atoms, forming a nearly tetrahedral configuration. Along the c axis the $Zn-O$ distance is smaller than for the other tree $Zn-O$ distances, 0.190 nm and 0.198 nm, respectively. This means that the centers of charge are not aligned at the same crystal points and this polarity gives ZnO a piezoelectric property.

[1] P indicates the primitive lattice that underlies the structure. The symmetry elements indicates a 6-fold screw axis, i.e a $360^\circ/6$ right-handed screw rotation counter clockwise, followed by a translation by 3/6. The structure also has a mirror plane and an axial glide plane with glide vector c/2 [4].

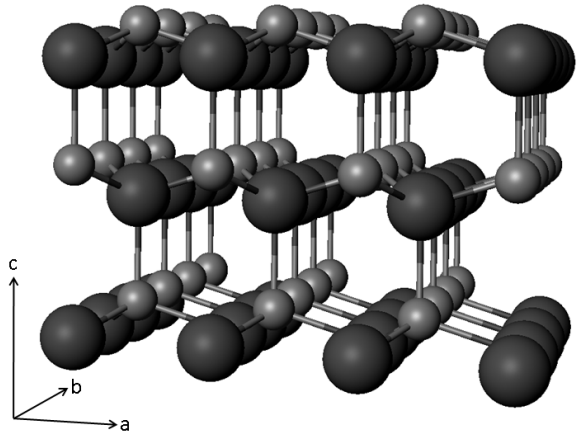

Figure 2.1: Perspective view of the wurtzite structure. The larger anions represent the oxygen atoms, and smaller cations the zinc atoms. The figure is created using Accelrys DS Visualizer 2.0.

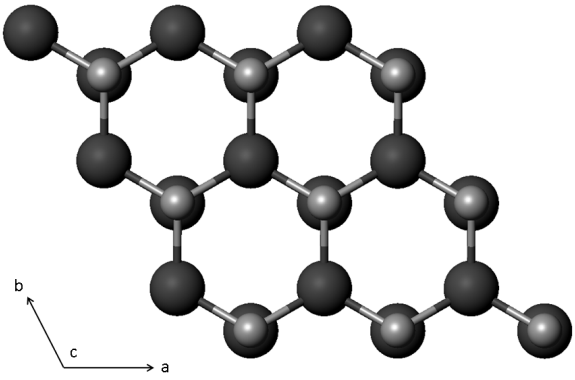

Figure 2.2: The wurtzite structure viewed along the *c* axis.

2.1.1 Zinc oxide synthesis

Some growth methods for ZnO crystals will be mentioned in this section, mainly hydrothermal growth (HT), since the single crystal samples investigated in this thesis are HT ZnO. Reference [5] is a good source for an introductory review of several growth techniques for ZnO.

ZnO powder is made from the combustion of vapor coming from the distillation of metallic zinc, the so-called French process. To synthesize high purity crystals, the pressurized melt-growth method can be used, where a melt of ZnO is held in a crucible with an oxygen overpressure ($\sim$50 atm). Ingots with up to 5.5-inch diameter have been reported, but small grain size is a drawback of the technique [6].

Another method is vapor growth, where small crystals can be obtained by chemical vapor transport (CVT) in closed tubes using chemical transport agents (Zn, $ZnCl_2$, etc.) at temperatures ranging from 800°C to 1150°C. The growth rates are about 40 μm per hour, and 2-inch diameter crystals have been reported [7].

2.1.1.1 Hydrothermal growth of ZnO

Hydrothermal growth uses an aqueous solvent, commonly NaOH, LiOH or KOH, at elevated temperatures and pressure to dissolve ZnO. By convection between two ZnO containing zones, the dissolution and the crystal zone, the crystal is grown from the dissolution. The temperature difference between the two zones are about $20 - 80$°C. Typical growth conditions are temperatures within $230 - 300$°C in the growth zone, and a pressure within $50 - 350$ MPa. The solvent is a mixed KOH + LiOH solution [8]. The advantages of HT are the low growth temperatures, and the reduction of most of the impurities in the source material, so high quality crystals can be grown. However, low growth rate ($\sim$250 μm per day), and incorporation of both OH and H_2O and the elemental components of the solvents into the crystal can be a disadvantage. Typically HT crystals contain concentrations of $10^{16} - 10^{18}$ cm^{-3} of Li, and $10^{16} - 10^{17}$ cm^{-3} of Cu, Mg, Si, Fe, Mn and Ag.

2.1.2 Transparent conductive oxides for electrode applications

Transparent conductive oxides (TCOs) made of doped wide band gap[2] semiconductors are materials that are both transparent and have low electrical resistivity. In principle wide band gap semiconductors are semi insulating at room temperature. However, high concentrations of charge carriers can be obtained by the use of two doping mechanisms, intrinsic and extrinsic doping.

Intrinsic doping is due to deviations in the crystal lattice. For instance oxygen deficiency leads to oxygen vacancies, which may give rise to shallow donor states below the conduction band and act as n-type dopants.

Extrinsic doping is crystal distortion by replacement of the original atoms. Substitution of the Zn atoms having higher valence, or substitution of oxygen atoms having lower valence can increase the carrier concentration.

In 1906 this transparent and conductive property was first observed in cadmium oxide [9], but technological advances emerged only after decades later. Indium oxide was identified as transparent and conductive in 1956 [10], and after years of extensive research tin doped indium oxide was found to have excellent electrical and optical properties for a TCO [11]. However, limitations of TCOs became critical as devices based on these materials got more sophisticated. The resistivity should decrease while maintaining the transparency. Simply increasing the thickness will not do, since optical absorption will follow Beer-Lambert's law [12] (equation 2.1) and increase exponentially with the thickness.

$$I_{\text{out}} = I_{\text{in}} e^{-\alpha d} \tag{2.1}$$

where I is the intensity of light, α is the absorption coefficient and d is the thickness. The conductivity, σ, is the product of the number of charge carriers, n, in the material, and the mobility, μ, of these carriers times the elementary electron charge, e,

$$\sigma = en\mu. \tag{2.2}$$

[2]The band gap energy, E_g, is the energy separation between the top of the valence band and the bottom of the conduction band.

Resistivity, ρ, is defined as the inverse of the conductivity. For thin uniform films, the electrical resistance can be expressed as the sheet resistance ($R_s = \rho/d$), so the lateral resistance is inversely proportional to the thickness. This implies that the resistance can be decreased by increasing the carrier concentration, mobility or film thickness. The carrier concentration, n can be increased by substitutional doping, creation of vacancies or interstitials, dependent on the material. However, this will affect the optical properties by an increase of the free carrier absorption. Another option is to increase μ, but, it depends on intrinsic scattering mechanisms and can not be controlled directly.

On the front side of a solar cell, a TCO can be used as a lateral charge conductor. In contrast to the present day metal contacts, the TCO is not shading the incident light. ZnO is one important material within this class of oxides, among tin doped indium oxide (In_2O_3:Sn) and fluorine doped indium oxide (SnO_2:F) abbreviated ITO and FTO, respectively. ZnO is typically doped using aluminium (AZO) or gallium (GZO). Their band gaps are >3.37 eV (see table 2.1), leading to transparency for light with wavelength <365 nm. With regard to energy, it is convenient to think of light as photons. Each photon carries the energy, E, given by

$$E = \frac{hc}{\lambda}, \tag{2.3}$$

where h is Planck's constant and λ is the wavelength. If the TCO is not utilized as a photo-active layer, a high optical transmission is required for light with E below the band gap of the TCO, and above the band gap of the photo-active cell. Silicon has a band gap of 1.12 eV at room temperature, which indicates a required transmission range from 365 - 1100 nm for TCOs applied on silicon based solar cells.

2.2 Examples of applications using zinc oxide

ZnO is a II-VI compound wide band gap semiconductor with several attractive electrical and optical properties. The 3.37 eV band gap [14] leads to transparency in the visible region, while the resistivity can be very low due

Parameter	ZnO	In_2O_3	SnO_2	Si	Unit
Mineral	Zincite		Cassiterite	Silicon	
Optical E_g	3.4 (d)	3.6 (d)	3.6 (d)	1.12 (i)	eV
Lattice	Hexagonal	Cubic	Tetragonal	Cubic	
Structure	Wurtzite	Bixbyite	Rutile	Diamond	
Space group	$P6_3mc$	$Ia3$	$P4_2/nmm$	$Fd3m$	
a, c	0.325, 0.5207	1.012	0.474, 0.319	0.5431	nm
Density	5.68	7.12	6.99	2.33	g cm^{-3}
Melting T	1,975	1,910	1,620	1,410	°C

Table 2.1: ZnO in comparison to In_2O_3, SnO_2 and silicon. A summary from [13]. d: direct and i: indirect band gap.

to intrinsic or extrinsic charge carriers. This makes it a suitable material for a number of different applications, as discussed below.

2.2.1 Solar cell and flat-panel displays with ZnO

For amorphous silicon solar cells, ZnO is frequently being used as a front contact. ZnO also plays an essential role as a textured back reflector where it minimizes reflection losses and can provide an effective light trapping [15]. In $CuInGaSe_2$ (CIGS) [16], CdTe [17] and organic [18] solar cells AZO have been used as a transparent conducive layer showing promising results. In flat-panel displays tin doped indium oxide is frequently used today. However, cost and limited availability of indium has led to a strong interest in replacing ITO by other materials. ZnO may be a serious alternative [19]. Several types of thin film solar cells apply ZnO as a TCO. Some configurations are schematically shown in figure 2.3.

2.2.2 ZnO varistors

ZnO varistors were developed in the 1970s [20]. A varistor is an electronic component that has a voltage dependent resistance. The name comes from "variable resistor", and it is used for over-voltage protection of electronic circuits. This special property is governed by oxide additives as Bi_2O_3 and

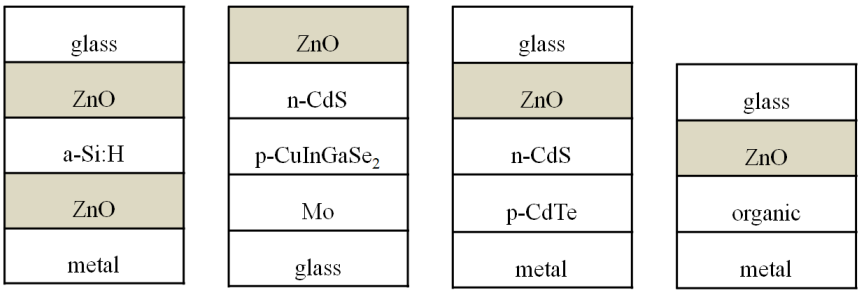

Figure 2.3: Cross sectional sketch of different thin film solar cell design with transparent conductive ZnO. From left: amorphous silicon, CIGS, CdTe and an organic solar cell.

Sb_2O_3, which segregate to the grain boundaries during sintering, and lead to a large barrier for electron transport.

2.2.3 ZnO piezoelectrics

The piezoelectric property of ZnO makes it applicable to several devices, like a surface-acoustic wave (SAW) device or piezoelectric sensors [21]. The discovery of this piezoelectricity led to the first electronic application of ZnO, as a thin layer for SAW devices [22]. The effect is due to the fact that ZnO has the ability to generate an electric potential in response to an applied mechanical stress. In a SAW device, an electrical contact induces an acoustic wave traveling along the surface that can be detected by another contact. This effect is typically used in band pass filters; devices which only let frequencies within a specified range pass, and block every frequencies outside that range [23].

2.2.4 ZnO thin-film transistors

Recently, transparent thin-film transistors (TTFTs) were reported based on the In-Ga-Zn-O (a-IGZO) system, showing promising results [24]. TTFTs present the opportunity to create flexible microelectronics that are both invisible and/or work at high temperatures [25].

2.2.5 Spintronics

A prospective use of ZnO is within spintronics (spin electronics). Alloying ZnO with transition elements like chromium, manganese, cobalt or nickel one can prepare diluted magnetic semiconductors. The magnetic 3d transition metal ions cause an exchange interaction between sp-electrons and the d-electrons. Localized electron spin at the magnetic ions gives magnetic-field-induced application possibilities, which use the spin of the electrons for electronic devices [26, 27]. Both storage and manipulation of information using spin states may prove practical for quantum computing and computer memory applications [28, 29].

2.2.6 Light emitting ZnO

Another interesting quality of ZnO is its high exciton binding energy (60 meV) [30], which makes it a good candidate for short wavelength light emitting diodes (LEDs), OLEDs [31] and lasers [32, 33]. The intense interest in replacing the competing GaN-based optoelectronic devices, has led to a major driving force of research on ZnO [34].

2.2.7 Non-electronic applications of ZnO

ZnO in the form of powder is also used in many non-electronic applications like paint, agriculture and rubber production. Nano particles of ZnO is used in sunscreens as a physical filter, because of its excellent properties as a UV-light absorber and scatter [35].

2.3 Electrical properties and doping of ZnO

2.3.1 Intrinsic dopants

ZnO exhibits in most cases, regardless of growth technique, *n*-type conductivity with carrier concentration in the $10^{15}-10^{17}$ cm^{-3} range [36]. Even lithium-rich hydrothermally grown ZnO may have carrier concentration in the $10^{12}-10^{13}$ cm^{-3} range, being semi-insulating [37]. This unintentional *n*-type conductivity is one of the main questions regarding ZnO. For some

time there has been speculation about the origin. Oxygen vacancies (V_O) and zinc interstitials (Zn_i) were assumed to be the dominant native defects causing *n*-type ZnO [38], simply because interstitial Zn-cations provide electrons, and O-anions provide holes.

Recently, Janotti and Van de Walle [39] performed computer modeling of native defects in ZnO. Using first-principles methods based on density functional theory within the local density approximation, they reported that these native defects are unlikely the cause of the unintentional *n*-type conductivity. Their results show that V_O has high formation energy in *n*-type ZnO, and is a deep donor with a very high ionization energy. Zn_i was found to be a shallow donor, but it also has a high formation energy in *n*-type ZnO. In addition, Zn_i is a fast diffuser with a migration barrier equal to 0.57 eV, and thus unlikely to be stable in *n*-type ZnO. The zinc antisites (Zn_O) was also found to be shallow donors, but with high formation energies, even in zinc rich conditions. However, under nonequilibrium conditions like irradiation, Zn_O may play a role, as a low-energy atomic configuration was identified. Zinc vacancies (V_{Zn}) are assigned to deep acceptors, and act as compensating centers in *n*-type ZnO. Oxygen interstitials (O_i) act also as deep acceptors at octahedral interstitial sites but display high formation energies and are not expected to exist in significant concentrations. Oxygen antisites (O_{Zn}) are deep acceptors and have the highest formation energies of the acceptor type intrinsic defects. Concluding that despite the shallow level of Zn_i, it cannot be the only dominating donor. A schematic summary of the energy levels attributed to intrinsic defects in *n*-type ZnO, according to ref. [39] is given in table 2.2.

2.3.2 Extrinsic dopants

2.3.2.1 Donor type

Extrinsic *n*-type doping of ZnO has been investigated for decades, and now reproducible and reliable *n*-type doping of ZnO is relatively easy. TCO films using ZnO:Al were prepared by RF-magnetron sputtering by Wasa *et al* [40] in 1971 and indium doped ZnO was obtained using spray pyrolysis by Chopra *et al* [41] in 1983, both with resistivities of the order of 10^{-4} Ωcm.

Defect	Band gap position
V_{Zn}	deep acceptor
V_O	deep donor
Zn_i	shallow donor
O_i	deep acceptor
Zn_O	shallow donor
O_{Zn}	deep acceptor

Table 2.2: First estimate of band gap position of intrinsic defects in *n*-type ZnO. From [39].

Minami *et al* [42] also prepared group III element doping with B, Al, Ga or In in the 1980s. These elements have one electron more in the outer electron shell compared to zinc, and are efficient donors if they reside on a zinc-site in the lattice, according to equation 2.4.

$$D^\circ \rightleftharpoons D^+ + e^-, \tag{2.4}$$

where D° and D^+ are the neutral and ionized donor, respectively. At room temperature, the equilibrium is on the right-hand side of this equation. Later ZnO *n*-doped with group IV elements such as Si, Ge, Ti, Zr or Hf was prepared by RF-magnetron sputtering [43]. Recently Hu and Gordon [44] obtained *n*-type ZnO by doping with group VII element fluorine (F), where F was incorporated on an oxygen site. Even rare-earth element scandium (Sc) and yttrium (Y) were found to govern *n*-type conductivity in ZnO [45].

2.3.2.2 Acceptor type

Preparing consistent, reliable and low-resistivity *p*-type ZnO has proven quite a challenge. Even though, the concept does not seem to be too complicated. The intention has been to substitute zinc atoms with group I (Li, Na, K) or oxygen atoms with group V (N, P, As, Sb) elements. Then the substituted lattice sites get fewer valence electrons, and provide holes for *p*-type conductivity, as given in equation 2.5.

$$A^\circ \rightleftharpoons A^- + h^+, \tag{2.5}$$

where A° and A^{-} are the neutral and ionized acceptor, respectively. However, the dopant energy position is not shallow, and the solubility is low. Also, the dopants can show an amphoteric behaviour where it acts as acceptor on one lattice site and donor at other sites. For instance, lithium shows this property where Li_{Zn} is an acceptor, and Li_i is a donor [46, 47]. However, calculations show that Li_{Zn} is less stable than Li_i and that the acceptor level is relatively deep [48]. Li doping actually produces semi-insulating ZnO [49]; it may involve the formation of both Li_i and Li_{Zn} keeping the Fermi level close to the middle of the band gap. This mechanism could also hold for Na doping. Calculations suggest that K doping will be compensated by V_O and prevent the sample from transforming to *p*-type [50]. *p*-doping using As is also a challenge since As mainly resides on Zn-sites instead of O-sites [51]. The mismatch in ionic radii for P^{3-} (2.12 Å), As^{3-} (2.22 Å) and Sb^{3-} (2.45 Å) as compared to O^{2-} (1.38 Å), could be the reason for limited solubility of these elements. It has been calculated that ZnO is not fully ionic, but exhibits a significant covalent character [52]. Therefore the size argument may not apply here. Nitrogen has the lowest ionization energy and does not form the donor like antisite N_{Zn} [50]. It is therefore a natural choice for an acceptor dopant and has been widely used in experiments. It has about the same ionic radius as that of oxygen, and measurements using electron paramagnetic resonance confirm that N substitutes for O in the lattice [53]. However, hole concentrations are still limited to the order of $\sim 10^{17}$ cm^{-3} [54], and even though N_O acts as an acceptor, N_2 on the same site acts as a donor compensating the acceptors. This was experimentally proved by extended X-ray absorption fine structure spectroscopy [55], after predictions by density functional calculations [56]. Although several papers have claimed preparation of *p*-type ZnO, but often the results were doubtful and the *p*-type property vanished after short time [57].

2.3.3 Hydrogen in ZnO

An alternative explanation for the *n*-type conductivity could be incorporation of unintentional donor impurities during growth. Hydrogen stands

out as a likely candidate [58]. It occurs exclusively in the positive charge state (H^+) in ZnO, and is not amphoteric as in most other semiconductors [59]. Studies of hydrogen-related defects in ZnO were pioneered in the 1950s where Mollwo [60] and Thomas and Lander [2] reported hydrogen as a donor in ZnO. They studied hydrogen diffusion in ZnO and showed that annealing in H_2 causes a significant increase in *n*-type conductivity. Hutson [61] performed Hall effect studies and confirmed that annealing in H_2 gives rise to a donor center.

In 2000 van de Walle "rediscovered" hydrogen as a donor in ZnO by density functional theory [58], and shortly after several experiments tested the predictions. For instance Hofmann *et al* [62] proved by electron paramagnetic resonance and Hall measurements that hydrogen is a shallow donor. The concentration of hydrogen varies depending on growth technique. Hydrogen is always present during growth, and diffuse easily into ZnO. Single crystals grown by chemical transport can have hydrogen concentration equal to 5×10^{16} cm^{-3}, while magnetron sputtered ZnO:Al films can have 1×10^{20} cm^{-3} [63]. Hydrogen is tightly bound to oxygen forming a OH bond with a length $\sim$1.0 Å. Using first-principles calculations Li *et al* [64] recently studied the atomic configurations of binding sites and vibrational frequencies (ω) of H in ZnO. This tetrahedrally coordinated semiconductor has different sites where hydrogen can reside. It can bind to an anion in two ways; in the bond center site (BC), or in the antibonding site (AB). In addition, there are two types of orientations for each site, parallel ($\|$) and perpendicular ($\perp$) as shown in figure 2.4.

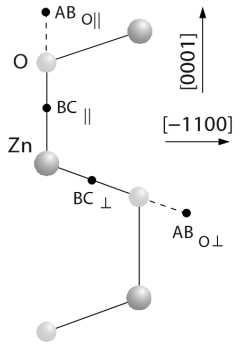

Figure 2.4: Schematic representation of four hydrogen sites in ZnO. From [64].

Site	ΔE (eV)	ω (cm^{-1})	d_{OH} (Å)
$BC_{\parallel}$	0.00	3421	0.985
$BC_{\perp}$	0.14	3505	0.985
$AB_{O,\parallel}$	0.19	3097	1.001
$AB_{O,\perp}$	0.15	3109	1.004

Table 2.3: Calculated formation energies relative to $BC_{\parallel}$ for hydrogen in ZnO, ω is the net vibrational frequency for hydrogen in ZnO [64].

The calculations suggest that all four sites have relatively low total energy, with $BC_{\parallel}$ as the lowest. However, the occupation of the BC sites by hydrogen requires displacements of the lattice atoms, which may not so often occur due to their relatively large masses with respect to that of hydrogen. Hence, hydrogen might occupy the AB_O sites instead, despite their higher energies. To differentiate among the configurations, calculation of the local vibrational modes (LVMs) might be helpful. In table 2.3 the suggested wavenumbers are represented.

In general the formation energy of hydrogen-related defects in *p*-type ZnO is lower compared to *n*-type. This may be beneficial for obtaining *p*-type ZnO since incorporation of hydrogen during growth can increase acceptor solubility, and even suppress formation of compensating defects [14]. Hydrogen has been shown to diffuse out of ZnO at 600° but without dramatic loss in free carrier concentration [65]. Therefore, the *n*-type conductivity may arise from multiple impurity sources and not from hydrogen alone [66, 67, 68]. Aluminium impurities have been suggested as an additional source for the unintentional *n*-type conductivity [69].

2.4 Basic theory of vibrational modes

The atoms that compose a crystal are bonded together and vibrate dependently of each other in collective modes. These oscillations exhibit quantized energies, and each unit of quantized vibrational energy is called a "phonon". If the perfect translational symmetry of the lattice is destroyed by an impurity, new vibrational modes may appear [70]. The new vibra-

tional mode is localized both spatially around the defect and in frequency space. Localized modes occur when a defect consists of an impurity atom lighter than the host atoms of the crystal. Introducing a heavier atom (or a lighter atom with weaker force constant), usually leads to modified band modes within the perfect lattice frequencies. The vibrational frequencies of localized modes are typically within the tera hertz (THz) region, hence it can couple with the electrical vector of infrared light. It can actually be observed as relatively sharp absorption lines in infrared spectroscopy. In the following sections, a description of vibrational properties in a perfect crystal lattice will be given. Later it will be modified to include how impurities affect vibrational modes.

2.4.1 The classical harmonic oscillator

First, let us derive the classical description of a particle constrained in a one dimensional periodic potential. The potential is given by

$$U(x) = U_0 + \frac{1}{2}kx^2, \tag{2.6}$$

where x is the particle's displacement from equilibrium and k is the spring constant. The force on the particle in the potential is then given by Hook's law;

$$F = m\frac{d^2x}{dt^2} = -kx \tag{2.7}$$

where m is the mass of the particle. The solution to this differential equation is

$$x(t) = A\cos(\omega t + \phi), \tag{2.8}$$

where A and ϕ are initial condition constants, and ω is the oscillation frequency given by

$$\omega = \sqrt{\frac{k}{m}}, \tag{2.9}$$

The kinetic energy of the system is given by

$$K = \frac{1}{2}m\left(\frac{dx}{dt}\right)^2 = \frac{p^2}{2m}, \tag{2.10}$$

where p is the momentum of the particle. The total energy of the system is thus

$$E = K + U = \frac{p^2}{2m} + \frac{1}{2}m\omega^2 x^2. \tag{2.11}$$

However, there is no such thing as a perfect harmonic oscillator. Stretching it too far will break the spring, and typically Hooke's law fails before that point is reached. On the other hand, in practice any potential is approximately parabolic in the neighbourhood of a local minimum.

2.4.2 The quantum harmonic oscillator

The quantum mechanical analogue of the classical harmonic oscillator is the quantum harmonic oscillator. Equation 2.11 does not satisfy the quantized requirements for the energy of atoms in a crystal lattice. Quantum mechanics must be applied to solve the quantum harmonic oscillator problem. Griffiths's "Quantum Mechanics" [71] has an extensive derivation, and the following is a short resumé. The quantum problem is to solve the Schrödinger equation for the potential U from equation 2.11. It is sufficient to solve the time-independent Schrödinger equation:

$$-\frac{\hbar^2}{2m}\frac{d^2\psi}{dx^2} + \frac{1}{2}m\omega^2 x^2\psi = E\psi \tag{2.12}$$

The momentum operator is $p \equiv (\hbar/i)d/dx$, so this equation can be rewritten as

$$\frac{1}{2m}[p^2 + (m\omega x)^2]\psi = E\psi. \tag{2.13}$$

Now the idea is to factor the Hamiltonian,

$$H = \frac{1}{2m}[p^2 + (m\omega x)^2]. \tag{2.14}$$

Since p and x are operators that do not commute, $a_\pm$ is defined to make the factorization easier:

$$a_\pm \equiv \frac{1}{\sqrt{2\hbar m\omega}}(\mp ip + m\omega x). \tag{2.15}$$

The factor in front has a cosmetic effect only on the final results. The product is

$$\begin{aligned} a_- a_+ &= \frac{1}{2\hbar m\omega}(ip + m\omega x)(-ip + m\omega x) \\ &= \frac{1}{2\hbar m\omega}[p^2 + (m\omega x)^2 - im\omega(xp - px)], \end{aligned} \tag{2.16}$$

and the extra term $(xp - px)$ is called the commutator. Typically written as $[x, p]$. Then

$$a_- a_+ = \frac{1}{2\hbar m\omega}[p^2 + (m\omega x)^2] - \frac{i}{2\hbar}[x, p] \tag{2.17}$$

It can be shown that $[x, p] = i\hbar$, which is called the canonical commutation relation. Then equation 2.17 becomes

$$a_- a_+ = \frac{1}{\hbar\omega}H + \frac{1}{2}, \tag{2.18}$$

or

$$H = \hbar\omega\left(a_- a_+ - \frac{1}{2}\right) = \hbar\omega\left(a_+ a_- + \frac{1}{2}\right). \tag{2.19}$$

Then, in terms of $a_\pm$ the Schrödinger equation takes the form

$$\hbar\omega\left(a_\pm a_\mp \pm \frac{1}{2}\right)\psi = E\psi. \tag{2.20}$$

If ψ satisfies the Schrödinger equation with energy E ($H\psi = E\psi$), then $a_+\psi$ satisfies the Schrödinger equation with energy $E + \hbar\omega$. That is

$$H(a_+\psi) = (E + \hbar\omega)(a_+\psi), \tag{2.21}$$

and

$$H(a_-\psi) = (E - \hbar\omega)(a_-\psi). \tag{2.22}$$

This can be applied to find new solutions with higher and lower energies. Simply by the $a_\pm$-ladder operators. However, to get started one ground state must be established. First, if

$$a_-\psi_0 = 0 \tag{2.23}$$

$\psi_0(x)$ can be determined:

$$\frac{1}{\sqrt{2\hbar m\omega}}\left(\hbar\frac{d}{dx} + m\omega x\right)\psi_0 = 0 \tag{2.24}$$

or

$$\frac{d\psi_0}{dx} = -\frac{m\omega}{\hbar}x\psi_0. \tag{2.25}$$

The solution to this differential equation is

$$\psi_0(x) = Ae^{-\frac{m\omega}{2\hbar}x^2}, \tag{2.26}$$

where A is the normalization constant. Normalizing gives

$$1 = |A|^2 \int_{-\infty}^{\infty} e^{m\omega x^2/\hbar}\, dx = |A|^2 \sqrt{\frac{\pi\hbar}{m\omega}}, \tag{2.27}$$

so $A^2 = \sqrt{m\omega/\pi\hbar}$ and hence the ground state of the quantum harmonic oscillator becomes

$$\psi_0(x) = \left(\frac{m\omega}{\pi\hbar}\right)^{1/4} e^{-\frac{m\omega}{2\hbar}x^2}. \tag{2.28}$$

The energy of this state can be determined by plugging it into the Schrödinger equation in equation 2.20, and exploit equation 2.23:

$$E_0 = \frac{1}{2}\hbar\omega. \tag{2.29}$$

Now, the excited stated can be generated by applying the raising operator repeatedly, increasing the energy by $\hbar\omega$ with each step:

$$\psi_n(x) = A_n (a_+)^n \psi_0(x), \tag{2.30}$$

with quantized energies of the quantum harmonic oscillator

$$E_n = \left(n + \frac{1}{2}\right)\hbar\omega. \tag{2.31}$$

Further it can be shown that the wave function for each state is

$$\psi_n = \frac{1}{\sqrt{n!}} (a_+)^n \psi_0, \tag{2.32}$$

where the normalization factor in equation 2.30 is $A_n = 1/\sqrt{n!}$.

2.4.3 The approximation of a general potential

The harmonic potential can only be used as an approximation, since it does not describe the exact potential of an atom in a crystal lattice. If the general potential $U(x)$, which has an equilibrium at $U(0)$, is Taylor expanded it becomes:

$$U(x) = U_0 + \left.\frac{dU}{dx}\right|_{x=0} x + \frac{1}{2!}\left.\frac{d^2U}{dx^2}\right|_{x=0} x^2 + \frac{1}{3!}\left.\frac{d^3U}{dx^3}\right|_{x=0} x^3 + \dots \tag{2.33}$$

Now, the first term is a constant and the second term is zero, since that is a condition of a stable equilibrium. The third therm is the harmonic term,

and beyond are the higher order terms. When considering small displacements in x, the higher order terms have negligible effect compared to the harmonic term. This is why the harmonic oscillator can be used as an approximation for the vibrational properties of materials. However, some details cannot be explained by the harmonic oscillator. They are classified as anharmonic effects since real potentials exhibit anharmonicity. One model that attempts to compensate for this deviation is the Morse potential [72] given by

$$U(x) = D_e(1 - \exp(-\beta x)))^2, \tag{2.34}$$

where D_e is the binding energy, $x = r - r_0$ (i.e., the extension of the bond from its equilibrium distance) and β is a constant. For small x the Morse potential approximates the harmonic potential, with a spring constant $k = 2D_e\beta^2$. Then

$$E_n = \omega_e \left(n + \frac{1}{2}\right) - \omega_e x_e \left(n + \frac{1}{2}\right)^2, \tag{2.35}$$

where the vibrational quantum number

$$\omega_e = \beta \left(\frac{\hbar D_e}{\pi c \mu}\right)^{\frac{1}{2}}, \tag{2.36}$$

and

$$\omega_e x_e = \frac{\hbar \beta^2}{4\pi c \mu} \tag{2.37}$$

with μ as the reduced mass of the particle, and x_e as a constant accounting for the anharmonicity. This will be applied later when discussing a simple approximation of the O-H vibrational mode.

2.4.4 Crystal vibrations and linear chains of atoms

A crystal is a periodic arrangement of atoms bonded together repeatedly in three dimensions. At a finite temperature each atom has an equilibrium position where the net force from every surrounding atoms in the crystal equals zero. If an atom is perturbed from this position, the net force reacts and restores the atom to its equilibrium position. The mechanism responsible for vibrations in crystals is this restoring force, caused by covalent bonds or ionic attraction and repulsion. In the following sections a

treatment on vibrational properties of one-dimensional atom arrays will be given, including both monoatomic and diatomic chains, as treated by Kittel [73].

2.4.4.1 Monoatomic linear chain

This derivation of a model that describes vibrations in a crystal starts with a simplified model. The easiest set-up is that of a linear chain of atoms with the same mass and the same force constant between the atoms (see figure 2.5).

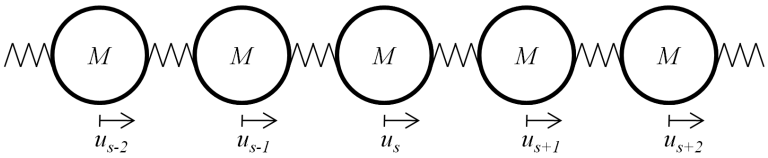

Figure 2.5: A monoatomic linear chain of atoms with mass M.

It can be used to approximately model lattice vibrations propagation along the [100]-, [110]- and [111]-directions in a cubic crystal with a one-atom basis. This model will find the frequency of the elastic wave in therms of the wavevector and elastic constants. When a wave propagates along one of these directions, entire planes of atoms move in phase with displacements either parallel or perpendicular to the direction of the wavevector. The displacement of the atom s from its equilibrium position is denoted u_s. The force on atom s from the displacement of atom $s + p$ is proportional to the displacements $u_{s+p} - u_s$. If only nearest-neighbor interactions are considered ($p = \pm 1$), the total force on s is

$$F_s = C(u_{s+1} - u_s) + C(u_{s-1} - u_s), \tag{2.38}$$

where C is the force constant. The equation of motion for atom s is

$$M\frac{d^2u_s}{dt^2} = C(u_{s+1} + u_{s-1} - 2u_s), \tag{2.39}$$

where M is the mass of the atom. The atoms oscillate with time dependence $e^{-i\omega t}$, and equation 2.39 becomes

$$-M\omega^2 u_s = C(u_{s+1} + u_{s-1} - 2u_s). \tag{2.40}$$

Considering displacements, u, of the propagating wave, solutions can be written in the form of

$$u_s = ue^{isKa}, \tag{2.41}$$

where a is the spacing between atoms and K is the wavevector. Inserting equation 2.41 into equation 2.40 yields

$$-\omega^2 Mue^{isKa} = C(ue^{i(s+1)Ka} + e^{i(s-1)Ka} - 2e^{isKa}), \tag{2.42}$$

and canceling u e^{isKa} from both sides leaves

$$\omega^2 M = -C(e^{iKa} + e^{-iKa} - 2). \tag{2.43}$$

Using the identity $2\cos Ka = e^{iKa} + e^{-iKa}$, gives the dispersion relation $\omega(K)$

$$\omega^2 = \left(2\frac{C}{M}\right)(1 - \cos Ka). \tag{2.44}$$

By the trigonometric identity, $1 - \cos Ka = 2\sin^2 \frac{Ka}{2}$, this may be written in the more common form

$$\omega(K) = 2\sqrt{\frac{C}{M}}\left|\sin\frac{Ka}{2}\right|. \tag{2.45}$$

Figure 2.6 shows a plot of this dispersion relation.

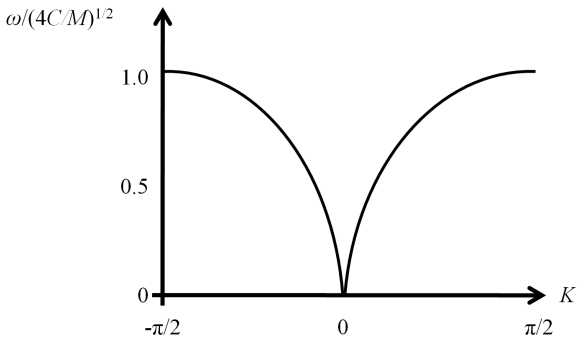

Figure 2.6: A plot of the dispersion relation, ω versus K, for a monoatomic linear chain of atoms.

2.4.4.2 Diatomic linear chain

The dispersion relation shows new features for crystals with two atoms in the basis. The simplest model is a diatomic linear chain with two types

of atoms, with different masses M and m, located at positions u_s and v_s, respectively (see figure 2.7). Again, only nearest neighbor interactions are

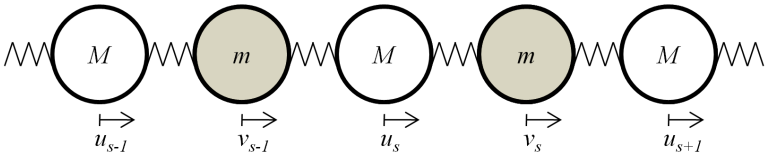

Figure 2.7: A diatomic linear chain of atoms with mass M and m.

considered. That is, the atom at position v_1 has mass m and interacts only with the atoms located at positions u_1 and u_2 with mass M. Then the equations of motion are given as

$$M\frac{d^2u_s}{dt^2} = C(v_s + v_{s-1} - 2u_s); \tag{2.46}$$

$$m\frac{d^2v_s}{dt^2} = C(u_{s+1} + u_s - 2v_s), \tag{2.47}$$

where s represents the unit cell where the two atoms reside. The solutions are in the form of propagating waves, now each atom will experience a different amplitude of oscillation

$$u_s = ue^{isKa}e^{-i\omega t}; \quad v_s = ve^{isKa}e^{-i\omega t}. \tag{2.48}$$

Substituting this into equation 2.46 and 2.47 gives

$$-\omega^2 Mu = Cv[1 + e^{-iKa}] - 2Cu; \tag{2.49}$$

$$-\omega^2 mv = Cu[1 + e^{iKa}] - 2Cv. \tag{2.50}$$

The linear equations have a solution only if the determinant is zero

$$\begin{vmatrix} 2C - M\omega^2 & -C[1 + e^{iKa}] \\ -C[1 + e^{iKa}] & 2C - m\omega^2 \end{vmatrix} = 0, \tag{2.51}$$

or

$$Mm\omega^4 - 2C(M + m)\omega^2 + 2C^2(1 - \cos Ka) = 0 \tag{2.52}$$

This can be solved for ω^2, obtaining

$$\omega^2 = C\left(\frac{1}{M} + \frac{1}{m}\right) \pm C\sqrt{\left(\frac{1}{M} + \frac{1}{m}\right)^2 - \frac{4}{Mm}\sin^2\left(\frac{Ka}{2}\right)}. \tag{2.53}$$

For a given value of K there are two angular frequencies, ω, corresponding to the positive and negative value of the second term. For instance by examining the limiting cases where $Ka \ll 1$ and $Ka = \pm\pi$ at the zone boundary; for small Ka, $\cos Ka \cong 1 - \frac{1}{2}K^2a^2 + \ldots$, and the two roots are

$$\omega^2 \cong 2C\left(\frac{1}{M} + \frac{1}{m}\right); \tag{2.54}$$

$$\omega^2 \cong \frac{\frac{1}{2}C}{M+m}K^2a^2. \tag{2.55}$$

Equation 2.54 represents the optical branch since the long wavelength optical modes in ionic crystals can interact with electromagnetic radiation. Equation 2.55 represents the acoustic branch since its dispersion relation is of the form characteristic of sound waves. For $K_{max} = \pm\pi/a$ the roots are

$$\omega^2 = \frac{2C}{M}; \quad \omega^2 = \frac{2C}{m}. \tag{2.56}$$

The dependence of ω on K for $M > m$ is shown in figure 2.8.

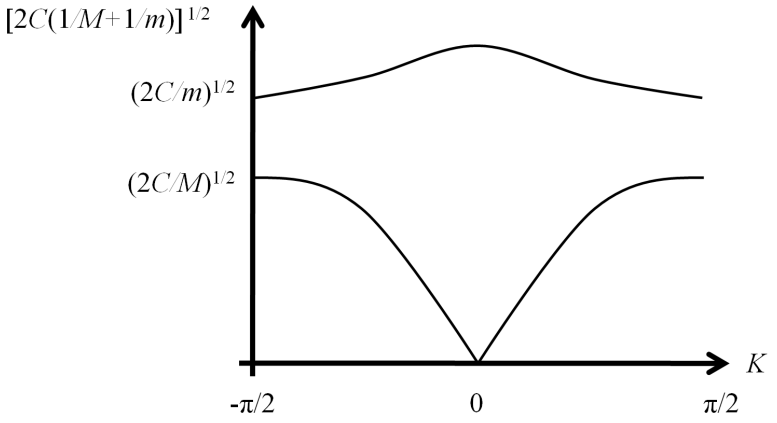

Figure 2.8: The dispersion relation for a diatomic linear chain with $M > m$. Showing the optical (top) and acoustical branches.

For the optical branch at $K = 0$, substitution of equation 2.54 in 2.49 gives

$$\frac{u}{v} = -\frac{m}{M}. \tag{2.57}$$

This shows that the two types of atoms have opposing velocities in the optical branch. The particles displacements in the transverse optical branch are shown in figure 2.9. A motion of this type can be excited by the electric field of a light wave, and is thus called the optical branch.

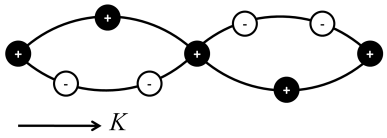

Figure 2.9: Transverse optical wave in a diatomic linear lattice, illustrated for two modes at the same wavelength.

2.4.5 The local vibrational mode

When a point defect is introduced into the crystal, the translational symmetry of the crystal is broken, and the normal vibrations of the lattice are slightly modified. Depending on the effective mass of the crystal defect, new modes appear either in the bands of allowed frequencies (band modes), at frequencies either greater than the maximum perfect lattice frequency (localized modes) or between the bands of allowed frequencies (gap modes). If the crystal defect is an impurity atom lighter than the host atoms, it leads to localized modes. As the term indicates, these modes are highly localized spatially around the defect. They cannot propagate throughout the crystal since the amplitude of any disturbance decreases exponentially with the distance from the defect [70]. This can be considered in a qualitative manner when studying the effects of introducing an isotopic impurity atom into the atomic chain. The local force constants are assumed to be unchanged. Then there are two possibilities, m' replaces m or M' replaces M.

If $m' < m$, a high frequency mode would rise out of the top of the optical branch at $K = 0$ with a frequency given by

$$\omega_L = \left[2C\left(\frac{1}{m'} + \frac{1}{\alpha M}\right)\right]^{\frac{1}{2}} \tag{2.58}$$

where the parameter $\alpha \to 1$ as $m' \to m$, and $\alpha \to 2$ as $m' \to 0$. In the first case the amplitudes of vibration of all atoms are essentially zero, except for the impurity and immediate neighbours. In the limiting value of $\alpha = 2$, no gap mode is expected since all atoms of mass m are stationary in the mode with the highest frequency in the acoustic branch. If $m' > m$, no localized mode is expected, but a mode of frequency equal to

$$\omega_G = (2C/m')^{\frac{1}{2}} \tag{2.59}$$

should fall into the gap below the optical branch.

Similar arguments can be made for the case where M' replaces M. If $M' < M$ there will be a localized mode

$$\omega_L = \left[2C\left(\frac{1}{m} + \frac{1}{\alpha M'}\right)\right]^{\frac{1}{2}} \tag{2.60}$$

and in addition there will be a gap mode from the top of the acoustic branch. On the other hand, $M' > M$ predicts no local or gap modes.

2.4.5.1 A model of an interstitial impurity

A simple model of the vibrational properties of an interstitial impurity can be approximated when considering the harmonic motion of two masses attached by a spring. The defect is assumed to behave as a semi-particle, so interactions with the other lattice atoms is neglected. Two atoms with masses m_1 and m_2 are attached by a spring with force constant k and length l. According to Hook's law, the force applied by a spring is

$$F = -kx, \tag{2.61}$$

where x is the change in the length of the spring. The force applied to each mass can be written as

$$m_1\ddot{x}_1 = -k(x_1 - x_2 - d); \quad m_2\ddot{x}_2 = -k(x_1 - x_2 - d), \tag{2.62}$$

where x_1 and x_2 are the positions, d is the length of the spring in equilibrium, and $\ddot{x}_1$ and $\ddot{x}_2$ are the accelerations for masses m_1 and m_2, respectively. The change in length of the spring is $x = x_1 - x_2 - d$, so equation 2.62 is

$$m_1\ddot{x}_1 = -kx; \quad m_2\ddot{x}_2 = -kx, \tag{2.63}$$

and since $\ddot{x}_1 - \ddot{x}_2 = \ddot{x}$,

$$\ddot{x} = \frac{-kx}{m_1} - \frac{kx}{m_2} = -kx\left(\frac{1}{m_1} + \frac{1}{m_2}\right). \tag{2.64}$$

The reduced mass μ is known as

$$\mu = \left(\frac{1}{m_1} + \frac{1}{m_2}\right)^{-1}, \tag{2.65}$$

then equation 2.64 can be written as

$$\ddot{x} = \frac{-k}{\mu}x, \tag{2.66}$$

with a solution on the form

$$x(t) = A\sin(\omega t) + B\cos(\omega t), \tag{2.67}$$

where ω is the angular frequency. For initial conditions $x(0) = c$, and $\dot{x}(0) = 0$, the solution can be written as

$$x(t) = c\sin(\omega t). \tag{2.68}$$

ω can be determined by comparing it to the second derivate of equation 2.66:

$$\ddot{x}(t) = \omega^2 c\sin(\omega t) = \frac{-k}{\mu}x(t). \tag{2.69}$$

Finally ω is found as

$$\omega = \sqrt{\frac{k}{\mu}}. \tag{2.70}$$

The force constant can be determined by following the derivation of vibrations of molecules in Young and Freedman [74]. When two atoms are separated by a few atomic diameters, they exert attractive van der Waals forces on each other. On the other hand, if they are too close their valence electrons overlap and the van der Waals force between the atoms becomes repulsive. There can be a equilibrium distance between these limits at which two atoms form a molecule. If the atoms are displaced slightly from equilibrium, they will oscillate in a simple harmonic motion.

If the center of one atom is at the origin, and the other atom is a distance r away, the equilibrium distance between the centers is $r = R_0$. Experiments show that the van der Waals interaction can be described by a potential energy function

$$U = U_0\left[\left(\frac{R_0}{r}\right)^{12} - 2\left(\frac{R_0}{r}\right)^{6}\right] \tag{2.71}$$

where U_0 is the positive constant with units of joules. The force on the second atom is the negative derivate:

$$F_r = -\frac{dU}{dr} = U_0\left[\frac{12R_0^{12}}{r^{13}} - 2\frac{6R_0^6}{r^7}\right] = 12\frac{U_0}{R_0}\left[\left(\frac{R_0}{r}\right)^{13} - \left(\frac{R_0}{r}\right)^{7}\right]. \tag{2.72}$$

A plot of the potential energy is sketched in figure 2.10. Since the force is

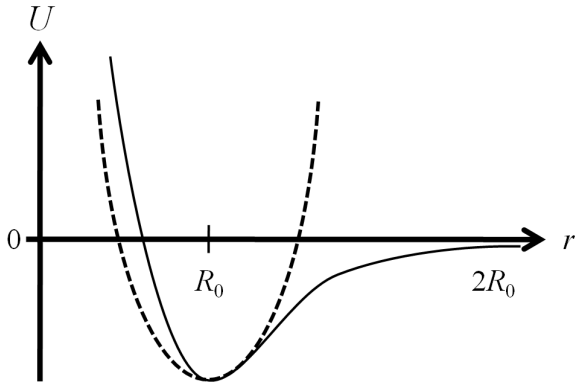

Figure 2.10: Potential energy U in the van der Waals interaction as a function of r. Dotted line illustrates the parabolic approximation used for small amplitude oscillations.

positive for $r < R_0$ and negative for $r > R_0$, it is a restoring force. The displacement x is introduced to study the oscillations around the equilibrium separation $r = R_0$:

$$x = r - R_0. \tag{2.73}$$

Then, in terms of x, equation 2.72 becomes

$$F_r = 12\frac{U_0}{R_0}\left[\left(\frac{R_0}{R_0+x}\right)^{13} - \left(\frac{R_0}{R_0+x}\right)^{7}\right] = 12\frac{U_0}{R_0}\left[\frac{1}{(1+x/R_0)^{13}} - \frac{1}{(1+x/R_0)^{7}}\right]. \tag{2.74}$$

Because only small amplitude oscillations are considered, the absolute value of the displacement x is small in comparison to R_0, and the absolute value of the ratio x/R_0 is much less than 1. The equation can then be simplified by using the binominal theorem:

$$(1+u)^n = 1 + nu + \frac{n(n-1)}{2!}u^2 + \frac{n(n-1)(n-2)}{3!}u^3 + \ldots \tag{2.75}$$

Each successive term is much smaller than the one it follows since $|u|$ is much less than 1, hence it is sufficient to use the two first terms to approximate $(1+u)^n$. Then

$$\frac{1}{(1+x/R_0)^{13}} = (1+x/R_0)^{-13} \approx 1 + (-13)\frac{x}{R_0}; \tag{2.76}$$

$$\frac{1}{(1+x/R_0)^7} = (1+x/R_0)^{-7} \approx 1+(-7)\frac{x}{R_0}; \tag{2.77}$$

and substituted for 2.74

$$F_r = 12\frac{U_0}{R_0}\left[\left(1+(-13)\frac{x}{R_0}\right)-\left(1+(-7)\frac{x}{R_0}\right)\right] = -\left(\frac{72U_0}{R_0^2}\right)x. \tag{2.78}$$

This shows that the force constant is approximately $k = 72U_0/R_0^2$.

2.4.5.2 Simple approximation of the O-H vibrational mode

Typically, the force constants for bond stretching can be found in tables, for instance in "CRC handbook of chemistry and physics" [75]. For the O-H stretching mode, the force constant is listed as $k = 780\ \mathrm{Nm}^{-1}$. There are three stable isotopes of oxygen, ^{16}O, ^{17}O and ^{18}O, with different properties (see table 2.4). However, it is assumed that ^{16}O is the isotope present in this approximation because of the high isotopic composition.

From the classical harmonic oscillator, the frequency in terms of wavenumbers is known as

$$\tilde{\nu} = \frac{1}{2\pi c}\sqrt{\frac{k}{\mu}} \tag{2.79}$$

where c is the speed of light. Calculation gives

$$\tilde{\nu} = \frac{1}{2\pi\, 3\times 10^{10}\ \mathrm{cm\ s}^{-1}} \times \sqrt{\frac{780\ \mathrm{Nm}^{-1}}{1.5629\times 10^{-27}\ \mathrm{kg}}}. \tag{2.80}$$

Canceling units (N=kg m $\mathrm{s}^{-2} \Longrightarrow \mathrm{Nm}^{-1}\mathrm{kg}^{-1} = \mathrm{s}^{-2}$) gives

$$\tilde{\nu} = \frac{1}{2\pi\, 3\times 10^{10}\mathrm{cm\ s}^{-1}} \times \sqrt{\frac{780\ \mathrm{s}^{-2}}{1.5629\times 10^{-27}}}; \tag{2.81}$$

$$\tilde{\nu} = 3747.9\ \mathrm{cm}^{-1}. \tag{2.82}$$

Nuclide	Mass (m_a/u)	Isotopic composition [at.%]
^{16}O	15.99491463	99.757
^{17}O	16.9991312	0.038
^{18}O	17.9991603	0.205

Table 2.4: Isotopic data for stable isotopes of oxygen. From webelements.com.

By applying the Morse potential for the anharmonic term (equation 2.35):

$$E_n = \omega_e \left(n + \frac{1}{2}\right) - \omega_e x_e \left(n + \frac{1}{2}\right)^2,$$

a more realistic $\tilde{\nu}$ can be approximated. The energy levels E_0, E_1 and E_2 can be calculated from this equation. The first and second states are given by

$$\Delta E_1 = E_1 - E_2 = \omega_e - 2\omega_e x_e; \tag{2.83}$$

$$\Delta E_2 = E_2 - E_0 = 2\omega_e - 6\omega_e x_e, \tag{2.84}$$

respectively. For now, values of $\omega_e x_e$ for O-H can be fond in tables, listed as $\omega_e x_e = 84.88\ \mathrm{cm}^{-1}$ [75]. From the above calculations, the anharmonicity constant $x_e = 44.16$, and the Morse approximation for the first exited state is

$$\tilde{\nu}_{1(\mathrm{OH})} = (3747.9 - 2 \times 84.88)\ \mathrm{cm}^{-1} = 3578.14\ \mathrm{cm}^{-1}, \tag{2.85}$$

and for the second state $\tilde{\nu}_{2(\mathrm{OH})} = 6986.52\ \mathrm{cm}^{-1}$.

2.4.5.3 Isotopic shifts in local vibrational modes

The models described up to now are only approximations, and other techniques are used for confirmation of the presence of a particular impurity. When studying local vibrational modes, one has the ability to narrow down what element could be responsible for the observed signal. One method is to introduce an isotope of the suspected impurity that will bond in the same manner in the crystal structure. Since the isotope has a different mass, the local vibrational mode will be different. The shift in frequency is called an isotopic shift and can be modeled quantitatively from the diatomic model. The most dramatic isotopic shift occurs when hydrogen is replaced by deuterium (D), where $m_{\mathrm{H}} = 1$ amu and $m_{\mathrm{D}} = 2$ amu. The crystal lattice is as usually treated as rigid with highly localized vibrational modes, so only nearest-neighbor atoms with mass M are considered movable, and the impurity with mass m is attached to the nearest atom by a spring with force constant k. From equation 2.70 the oscillation frequency of a diatomic model is

$$\omega = \sqrt{\frac{k}{\mu}} = \sqrt{k\left(\frac{1}{M} + \frac{1}{m}\right)}. \tag{2.86}$$

If the suspected local vibrational mode is caused by hydrogen, an isotopic substitution of deuterium would give rise to a shift of the vibrational mode. The ratio, r, between the former and the new frequencies for the O-H and O-D molecules becomes

$$r = \frac{\omega_H}{\omega_D} = \sqrt{\frac{k\left(\frac{1}{M} + \frac{1}{m_{\mathrm{H}}}\right)}{k\left(\frac{1}{M} + \frac{1}{m_{\mathrm{D}}}\right)}} = \sqrt{2\left(\frac{M+1}{M+2}\right)} = 1.3743, \tag{2.87}$$

where ω_H and ω_D represent the frequencies of the hydrogen and deuterium vibrational modes, respectively, and M is the mass of oxygen. The ratio in this case is slightly less than $\sqrt{2}$, which means that a hydrogen mode, ω_H, could be detected at approximately $\sqrt{2}$ times the deuterium mode, ω_D.

From the simple model in section 2.4.5.2, the first exited state of the OD mode should have $\tilde{\nu}_{(\mathrm{OD})} = \tilde{\nu}_{(\mathrm{OH})} \times r^{-1} \approx 2611\ \mathrm{cm}^{-1}$.

2.5 Previous work

Some of the previous work on infrared spectroscopy of ZnO will be presented in this section.

2.5.1 Infrared spectroscopy studies of hydrogen in ZnO

The presence of hydrogen-related donors in ZnO was confirmed by muon spin rotation (μSR) [76], electron paramagnetic resonance (EPR) and electron nuclear double resonance (ENDOR) [62]. Bond-centered (BC) and antibonding (AB) configurations were found to be close in energy for isolated interstitial H^+. However, the atomic configurations of these defects is still under debate.

Infrared spectroscopy can probe for local vibrational modes, and it is thus an excellent tool to study this problem. The vibrational frequencies of the LVMs reveal the chemical bonding of hydrogen with its neighbours, due to the dependence on the molecular structure of the hydrogen-related defects. Infrared absorption studies of hydrogen-related LVMs have been

done since the 1970's. Müller [77] and Gärtner and Mollwo [78, 79] investigated ZnO grown by vapor phase doped by copper and annealed in hydrogen or deuterium atmosphere (ZnO:Cu:H/D). They reported modes in the 3100 cm^{-1} and 2300 cm^{-1} regions for hydrogen- and deuterium-related defects, respectively.

Shortly after Van de Walle's publication in 2000 [58], it was a renewed interest in hydrogen-related LVMs in ZnO. McCluskey *et al* [80] reported an O-H stretch mode at 3326.3 cm^{-1} observed in nominally undoped vapor phase grown ZnO at 8 K after annealing in hydrogen atmosphere at 700°C (see figure 2.11).

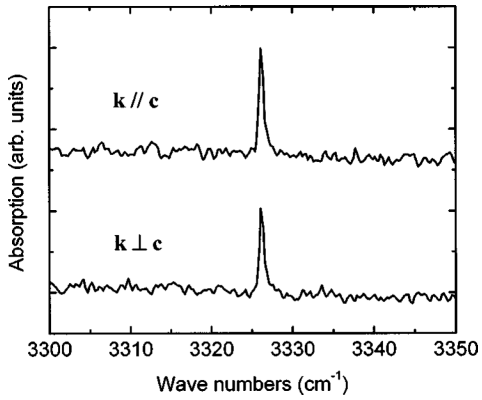

Figure 2.11: Infrared absorption spectra of the 3326.3 cm^{-1} O-H LVM in vapor phase grown ZnO at 8 K. The two spectra are offset vertically for clarity, showing absorption for light parallel to the *c* axis ($\mathbf{k}\|\mathbf{c}$) and perpendicular to the *c* axis ($\mathbf{k}\perp\mathbf{c}$). From McCluskey *et al* [80].

Van de Walle calculated O-H stretch modes frequencies at 3680 cm^{-1} and 3550 cm^{-1} for the bond-centered and antibonding configurations, respectively, for the harmonic approximations. To estimate the effect of anharmonicity, McCluskey *et al* used an approximation for OH-molecules in gas phase, where the stretch mode frequency shifts downward by 166 cm^{-1} [81]. Subtracting from the calculated frequency for the antibonding OH-complex yields a frequency of 3384 cm^{-1}, which is in reasonable agreement with the experimental observation. However, they did not fully rule out the bonding configuration, based on the uncertainty of the anharmonicity estimate. Further, they annealed a sample in deuterium atmosphere and

observed both free-carrier absorption at room-temperature (RT), and tentatively attributed an absorption peak at 2470.3 cm^{-1} to O-D complexes (see figure 2.12). This yields $r = 1.3465$ which is in good agreement with

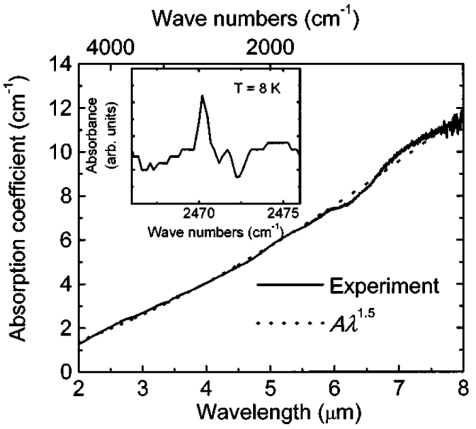

Figure 2.12: Infrared absorption of ZnO (at RT) annealed in deuterium gas. The inset shows a peak attributed to O-D complexes at 8 K. From McCluskey *et al* [80].

known *r*-values of complexes in GaP ($r = 1.3464$) [82]. Polarized light gave a peak maximum oriented at an angle of $\sim 110^\circ$ to the *c* axis providing conclusive evidence that the observations are consistent with hydrogen in an antibonding configuration.

2.5.1.1 The H-I, H-II and H-I* defects

Hydrogen-related defects in vapor phase grown undoped ZnO was studied by Lavrov *et al* in 2002 [83]. After exposure to hydrogen and/or deuterium plasma at $150 - 380^\circ$C for 2 hours, they observed new absorption lines at 3312.2, 3349.6 and 3611.3 cm^{-1} (see figure 2.13).

The LVM frequencies and the isotopic shifts ($r = 1.35$) suggest that the lines are stretch modes of OH absorbers. In the bottom spectra in figure 2.13, four additional lines at 2463.0, 2484.6, 3315.2 and 3346.6 cm^{-1} are observed when treated with both hydrogen and deuterium plasma, but no additional lines are seen near the 2668.0 and 3611.3cm^{-1} lines. This implies that (i) two different defects are responsible for the 3312.2, 3349.6 and 3611.3 cm^{-1} lines, (ii) the LVM at 3611.3 cm^{-1} originates from a defect containing

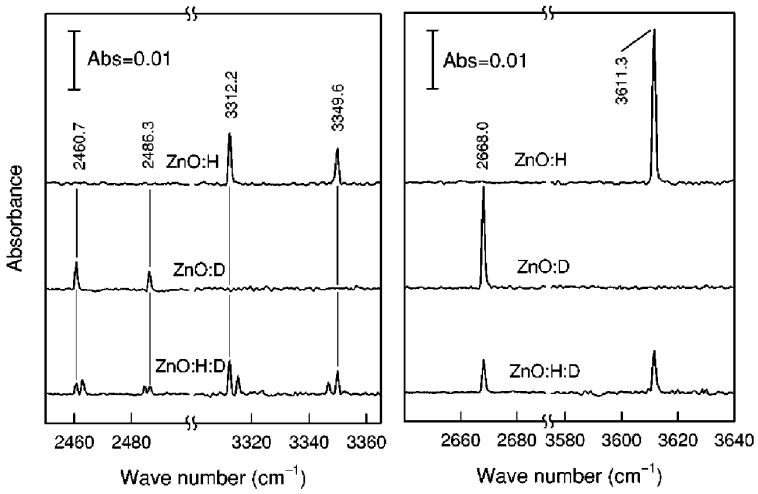

Figure 2.13: Infrared absorption of ZnO at 10 K after H-, D-, and (H+D)-plasma treatment. Using unpolarized light $\mathbf{k} \perp \mathbf{c}$. From [83].

one hydrogen atom, and (iii) the 3312.2 and 3349.6 cm^{-1} LVM's belong to a defect containing two non-equivalent hydrogen atoms. These two defects have been labeled H-I and H-II, respectively, and measurements of polarization dependences showed that the transition dipole moments responsible for the 3312.2 and 3611.3 cm^{-1} modes lie along the *c* axis, while the mode at 3349.6 cm^{-1} has a transition moment nearly perpendicular to *c*. Vibrational frequencies for several O-H configurations were calculated by Lavrov *et al* [83] using a more sophisticated DFT model from reference [58], and two tentative defect models were presented; the H-I defect is most likely an interstitial hydrogen at $BC_{\parallel}$, while the H-II defect is proposed a zinc vacancy having two hydrogen atoms, $V_{Zn}H_2$, in accordance with DFT calculations. The Zn vacancy is a double acceptor in *n*-type ZnO and occurs in the V_{Zn}^{2-} state, suggesting it can be neutralized by binding two hydrogen atoms.

Hydrothermal ZnO was later studied by the same group [84], reporting lines at 3335.6, 3482.0 and 3577.3 cm^{-1} in a virgin sample. These lines are also in the region of characteristic O-H stretch modes [75]. After a deuterium plasma treatment, a new line at 2644.4 cm^{-1} emerged, see figure 2.14. The dominating 3577.3 cm^{-1} line and the 2644.4 cm^{-1} line has an $r = 1.35$. No extra lines appeared in the spectra when the sample was

LVM (cm^{-1})	Configuration	Assignment	Reference
3191.6	O-H $\perp$ *c*	Cu$\cdots$O-H	[78, 79]
3312.2	O-H $\parallel$ *c*	$V_{Zn}H_2$	[83]
3326.3	O-H $\perp$ *c*	H_{BC}	[80]
3335.6	unknown		[84]
3349.6	O-H $\perp$ *c*	$V_{Zn}H_2$	[83]
3482.9	unknown		[84]
3577.3	O-H $\parallel$ *c*	Li$\cdots$O-H	[84, 85, 86, 87]
3611.3	O-H $\parallel$ *c*	H_{BC}	[83]

Table 2.5: LVM's in the region of characteristic O-H stretch modes observed in ZnO at 10 K.

treated with H+D plasma. Polarization measurements showed a dipole moment aligned along the *c* axis, indicating that the 3577.3 cm^{-1} vibration is due to a single O-H bond oriented along the *c* axis and a possible involvement of Li has been discussed by Lavrov *et al* [84]. This defect has been labeled H-I*. Table 2.5 summarizes reported modes and assignments suggested in the literature.

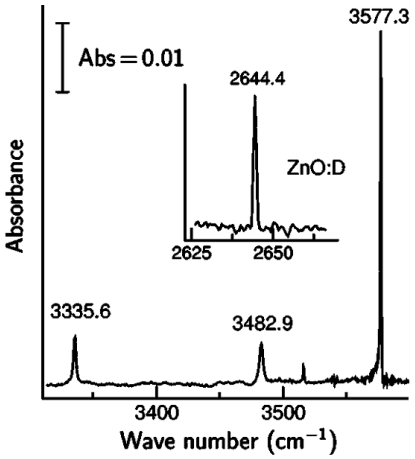

Figure 2.14: Absorption spectra of a virgin HT ZnO sample at 10 K using unpolarized light, $\mathbf{k}\perp\mathbf{c}$. Inset shows new line after two hours with D plasma at 350°C. From [84].

Chapter 3

Experimental techniques and instrumentation

In this chapter I will give a description of the investigated samples, the experimental procedure and a review of the main experimental technique used, Fourier Transform Infrared Spectroscopy (FTIR).

3.1 Samples

All the samples used in this thesis were cut form a single hydrothermally grown ZnO mono-crystalline wafer purchased from SPC Goodwill [88]. The ZnO single crystals were cut perpendicular ($\pm$ 0.25°) to the *c* axis. The oxygen terminated face ($000\bar{1}$) and Zn terminated face (0001) can be determined by identification flats, as illustrated in figure 3.1. Specifications are listed in table 3.1.

As mentioned in the previous section, HT ZnO is synthesized in a aqueous solvent containing LiOH. Hence, the samples had a high unintentionally concentration of lithium and were highly resistive. Secondary ion mass spectrometry (SIMS) measurements reported by Maqsood on equivalent as-grown samples revealed a Li concentration $\approx 10^{17}$ cm^{-3} [89]. When studying local vibrational modes in semiconductors by infrared spectroscopy, highly resistive samples are an advantage $-$ since the absorption by free carriers is minimized.

Figure 3.1: Sketch of a ZnO sample with the O-face upwards with physical dimensions 10x10x0.5 mm^3. Identification flats determines the orientation.

Parameter	Value
Dimensions	10x10x0.5 mm^3
Tolerance on thickness	$\pm$ 25µm
Purity	> 99.99%
Electrical resistivity	500-1000 Ωcm
Band gap at RT	3.37 eV

Table 3.1: Specifications of the ZnO samples according to SPC GoodWill [88].

3.2 Experimental procedure

A total of four samples were investigated by FTIR. Two types of detectors were used, DTGS and InSb, which will be described in the following sections. Two as-grown samples were studied, probing for hydrogen-related absorption lines. The third sample was implanted with hydrogen on both sides, each with an energy of 1.1 MeV and a dose 2×10^{16} cm^{-2}, and the fourth was implanted with deuterium on both sides each using an energy of 1.4 MeV and a dose 2×10^{16} cm^{-2}. Both implantations were performed at RT through a 15 µm thick Al foil, and these implantation conditions result in an implanted depth of ∼2.5 µm. Then FTIR measurements were repeated and the four samples were subsequently annealed for 70 hours at 400°C. FTIR measurements were again applied, probing for any changes in the hydrogen/deuterium related absorption lines. SIMS measurements were done on the D-implanted sample to study the deuterium and lithium concentration profiles. The deuterium implanted sample was used to determine any isotopic shifts in the LVMs. Table 3.2 summarizes the different process steps for all samples.

Sample	Step 1	Step 2	Step 3	Step 4	Step 5	Step 6
V85	FTIR	400°C @ 70 h	FTIR			
V104	FTIR	400°C @ 70 h	FTIR			
V91	FTIR	H-implantation	FTIR	400°C @ 70 h	FTIR	
V92	FTIR	D-implantation	FTIR	400°C @ 70 h	SIMS	FTIR

Table 3.2: An overview of all samples and processes done.

The samples V91 and V92 were hydrogen and deuterium implanted, respectively. Prior to implantation, they were investigated by FTIR measurements using the DTGS detector only and not the InSb one, which is more sensitive in the wavelength range of interest. This was because the InSb detector was not in operational condition at the early stage of this experiment. However, all the samples in table 3.2 came from the same wafer, and we expect an essentially identical distribution of defects and impurities. Consequently, it is reasonable to assume that all the four samples give identical infrared absorption spectra in the as-grown state. A photo of V104, V91 and V92 is given in figure 3.2.

Despite being rather thin, the highly damaged implanted region could produce detectable LVMs. We first measured the samples as-implanted and as-annealed. We then removed the implantation region by polishing away ≈15 μm, and measured the samples again, with only "as-grown and diffusion introduced" hydrogen/deuterium present.

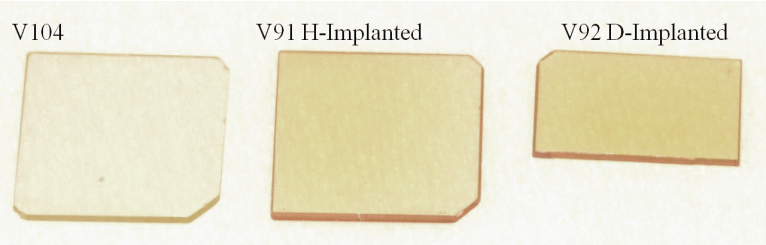

Figure 3.2: A photo of three ZnO samples. From left to right; an as-grown, a hydrogen implanted sample and a deuterium implanted sample. All of them have been annealed at 400°C for 70 hours. A piece of V92 was cut off for SIMS measurements.

3.2.1 Sample preparation

We always prepared the samples using a clean tweezer and gloves. Each sample was cleaned in three steps with acetone, ethanol and de-ionized water before the measurements in order to remove any contamination on the surface. Between measurements the samples were stored in a freezer at -18°C.

3.2.2 Sample mounting

Two custom made sample holders designed to fit on the "cold finger" of the cryostat were used in the FTIR measurements. The sample holder was a flat copper plate with a rectangular hole in the middle. The measurements were done at a sample temperature ∼15 K to avoid thermal effects on the spectra when probing for LVMs. All spectra were measured along two axes of the crystal, with the c axis both parallel ($\mathbf{k}\|c$) and perpendicular ($\mathbf{k}\perp c$) to the infrared beam. To minimize stress of the samples, they were very gently fixed on the sample holder. Since the samples were only 0.5 mm thick, mounting the samples for $\mathbf{k}\perp c$ spectra required aluminum tape to seal any stray light along the sample faces and to provide good thermal contact (see figure 3.3).

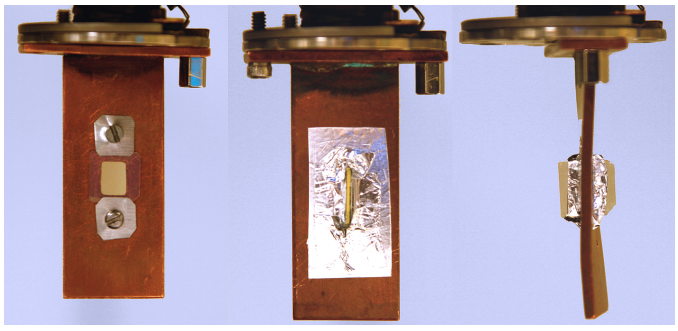

Figure 3.3: Portrait and cross-section picture of the sample holders with samples mounted. The tip if the "cold finger" can be seen on top. The first holder shows a sample oriented for $\mathbf{k}\|c$ measurements, second and third with sample oriented for $\mathbf{k}\perp c$ measurements. Aluminum tape was used to get good thermal contact and to seal any stray light.

3.3 Four point probe measurement

We measured the resistivity of the samples employing a four point probe set up (see figure 3.4). This technique employs four collinear probes. A current is passed between the two outer probes, and the voltage is measured across the two inner ones [90, 91]. The resistance associated with the voltage probes can be neglected, and the resistivity, ρ, is given as

$$\rho = 2\pi KP\frac{V}{I} \tag{3.1}$$

where K is a correction factor depending on the ratio of the sample thickness and the probe spacing, P. In our case $P = 0.067$ cm and $K = 0.74$.

Assuming that the mobility is known, the resistivity gives an estimate of the electron concentration, n, and the hole concentration, p, since

$$\frac{1}{\rho} = q(\mu_n n + \mu_p p) \tag{3.2}$$

where q is the charge and μ is the mobility [92].

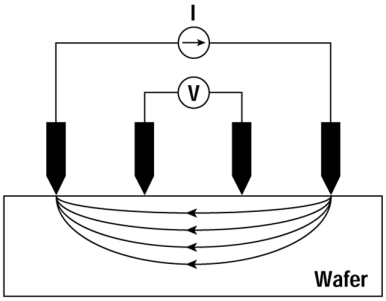

Figure 3.4: The collinear four point probe for determining the resistivity of a sample. From [93].

3.4 Fourier transform infrared spectroscopy

FTIR is a non-destructive optical method for both qualitative identification and quantitative determination of normal vibrational modes, impurities and defects in the material. In this section I will introduce the fundamental concept of FTIR, following the theory as given by Griffiths and De Haseth [94].

3.4.1 Brief introduction

Infrared (IR) spectroscopy is the study of how infrared light interacts with matter. The electrical vector of infrared light can couple with the electric dipole moment caused by vibrations in solids (as derived in previous sections), and the light with the energy equal to the vibrational frequency is absorbed, in accordance with the Beer-Lambert law.

A fraction of the infrared light at normal incidence will be reflected at the surface as stated by Fresnel's equations. Assuming a weak absorption, the reflectivity is

$$R = \frac{(n-1)^2}{(n+1)^2} \tag{3.3}$$

where n is the refractive index. In our case $n \approx 1.9$ for ZnO at infrared wavelengths [95], giving a surface reflectivity of about 10%.

The transmittance is given by

$$T = \frac{I}{I_0}, \tag{3.4}$$

where I_0 and I are the intensity of the incident and transmitted light, respectively, see figure 3.5.

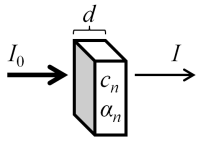

Figure 3.5: Diagram of Beer-Lambert Law, light propagating through a material with thickness d, with absorber concentration and absorption coefficient, c_n and α_n, respectively.

The absorbance is given as

$$A = -\mathrm{In}\frac{I}{I_0}, \tag{3.5}$$

where

$$A = cd\alpha. \tag{3.6}$$

However, not all molecular bonds are observable using infrared spectroscopy. There must be some degree of ionic interaction between the atoms,

and even then, not every modes are detectable. For instance a linear CO_2 molecule has three vibrational modes (see figure 3.6), but only two modes are IR-active.

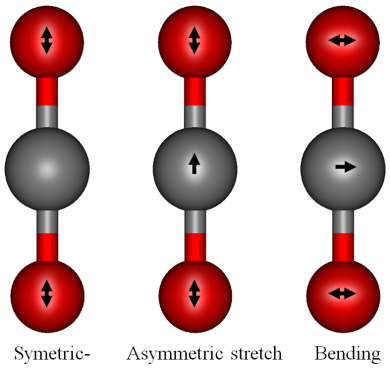

Figure 3.6: Three vibrational modes for a CO_2 molecule, illustrating the shifts in dipole moment. The symmetrical stretch mode induces no dipole, and is consequently IR inactive.

The amplitude of the electric vector of light changes over time and has the known shape of a sine wave. Wavenumbers are the most widely used unit in infrared spectroscopy to denote different frequencies of light. It is defined as the reciprocal of the wavelength:

$$\tilde{\nu} = \frac{1}{\lambda}, \tag{3.7}$$

where λ is the wavelength in cm. Then $\tilde{\nu}$ is a measure of the number of waves (crests or troughs) per cm. It is directly proportional to energy as:

$$E = hc\tilde{\nu}. \tag{3.8}$$

Different chemical bonds in molecules, known as functional groups, tend to absorb IR in the same wavenumber range regardless of the rest of the structure. For instance O-H stretch modes occurs "always" in the $3200 - 3600$ cm^{-1} region [96]. This correlation allows the modes to be identified from the infrared absorption spectrum, and is used in this thesis to determine the presence of hydrogen in ZnO.

3.4.2 Principles of operation

An infrared spectrum with intensity versus wavenumbers can be recorded in two ways. First, with a classical set-up of a dispersive spectrometer; a broadband IR beam is guided through a monochromator (a prism or grating), through the sample and finally to the detector which measures the intensity as a function of wavelength.

Second, one can employ a FTIR spectrometer, which has several convenient advantages. It is based on an interferometer and a mathematical operation: fourier transformation. A typical instrument is composed of an IR source, a Michelson interferometer and an IR detector (see set-up in figure 3.7).

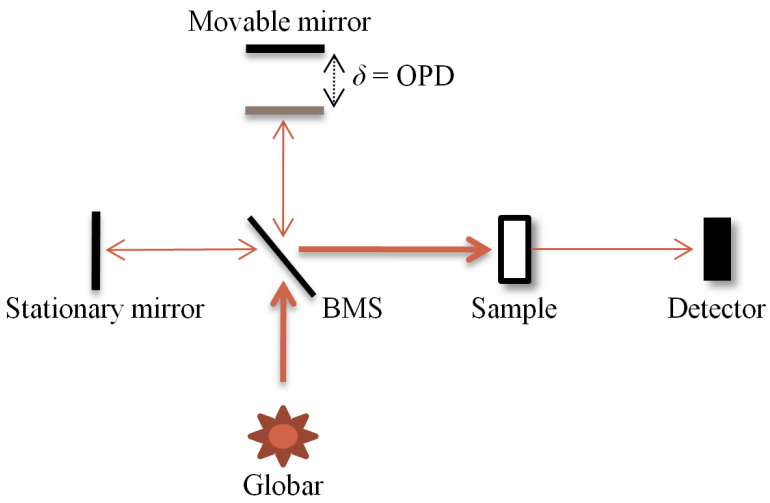

Figure 3.7: Schematic set-up of the main components in an FTIR spectrometer. BMS = beamsplitter and OPD = optical path difference.

The globar in figure 3.7 is a heated cylinder of silicon carbide (SiC) that emits a broad range of infrared radiation through black body radiation. The interferometer consists of a beamsplitter, a fixed mirror and a moving mirror (scanner). The beamsplitter separates the incident beam in two paths, and then recombines them after reflection by the two mirrors. One path length is fixed, and one path length can be varied by the scanner. If the two paths are of equal lengths, all frequencies of light will constructively interfere when recombined at the beamsplitter. At this condition the scanner is

positioned at the zero path difference. When the scanner is moved away from this position some frequencies will destructively interfere while other constructively interfere. Figure 3.8 shows the intensity output from the beamsplitter as a function scanner position, called an interferogram. The

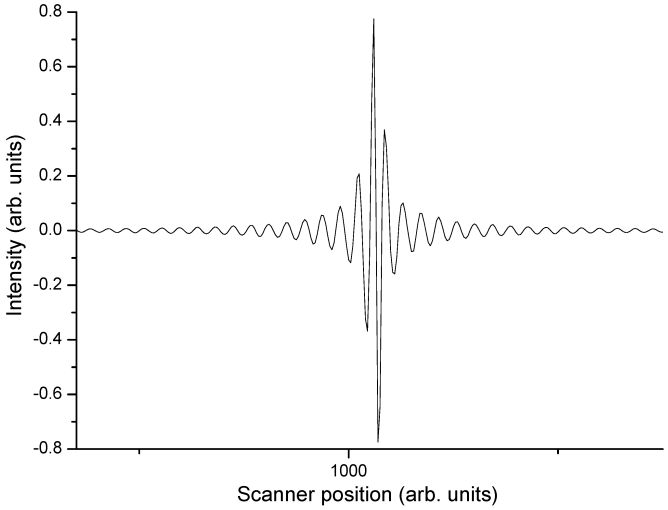

Figure 3.8: An example of an interferogram measured without sample (background spectrum). The center peak indicates the zero point difference position.

interferogram can be transformed to a infrared spectrum by calculating the fourier transform, as discussed in the next section. The fourier transform of the signal in figure 3.8 is given in figure 3.9. The background spectrum accounts for variations in the spectrum due to globar emission, beamsplitter and detector efficiency, and absorption features inherent to the spectrometer set-up. A transmission spectrum of a sample can be obtained in the same way by inserting a sample in front of the detector.Applying equation 3.5 and taking the ratio of the two spectra times the negative logarithm, an absorbance spectrum is given.

The resolution, Δ, of a spectrometer is given by:

$$\Delta \propto \frac{1}{\delta_{\max}} \tag{3.9}$$

where $\delta_{\max}$ is the maximum path difference, which is twice the mirror travel distance. Measurements performed in this thesis has a resolution of 1 cm^{-1}.

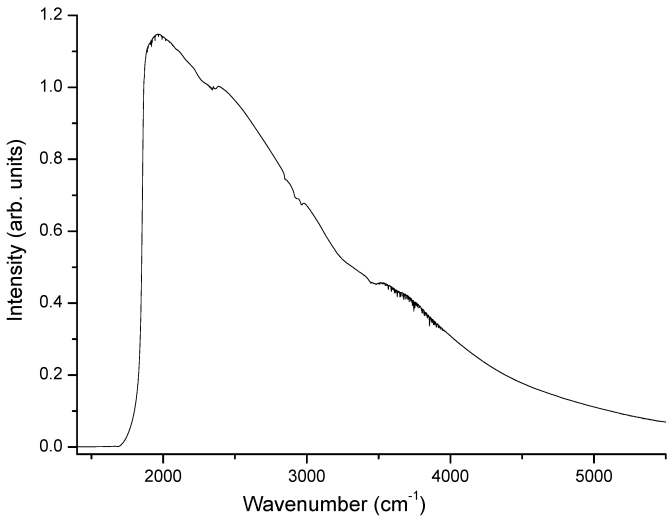

Figure 3.9: The fourier transform of the signal in figure 3.8, showing a background spectrum.

3.4.2.1 Beamsplitters

The purpose of the beamsplitter is to split the infrared beam into two parts, directing one reflecting part and one transmitted part to the mirrors. Different materials are used for specific range of frequencies. For mid-infrared ($400 - 4000$ cm^{-1}), a potassium bromine (KBr) beamsplitter with a thin germanium (Ge) coating gives a high efficiency. However, a calcium fluoride (CaF_2) beamsplitter with a silicon coating for wavenumbers in a range of $1250 - 15000$ cm^{-1} gives an even higher efficiency in the range $\gtrsim$3000 cm^{-1}.

3.4.2.2 Detectors

The detector converts the infrared radiation to an electrical signal. A commonly used thermal detector for the mid-infrared region is the ferroelectric DTGS detector (deuteriated triglycine sulfate). It has a permanent electric dipole because of the alignment of the molecules in the crystal. The faces of the crystal are oppositely charged, with a temperature dependent polarization. Its variation with temperature is called the pyroelectric effect. When the crystal absorbs infrared radiation the recorded change in voltage over

the crystal provides the detector signal.

A photovoltaic detector is a semiconductor pn-junction. The conductivity increases when infrared light excites electrons from the valence band to the conduction band. Both HgCdTe (mercury cadmium telluride) and InSb (indium antimony) are commonly used detectors. They have a narrow band gap and are cooled down using liquid nitrogen to reduce thermally excitation (noise) from the environment. Photovoltaic detectors have about $1-2$ orders of magnitude higher detectivity, compared to thermal detectors. However, they have a narrower region of operation, consequently more than one detector is needed for optimal measurements of broad spectral regions.

3.5 Fourier analysis

The Fourier analysis enables us to obtain the spectrum from the interferogram by taking the electric field as a function of scanner position, and Fourier transform it to the electric field as a function of frequency. The following is short resume of the derivation as outlined by Bell [97].

3.5.1 Derivation of the basic integral for Fourier transform spectroscopy

A Fourier pair $y(x)$ and $E(\tilde{\nu})$ can be represented as

$$y(x) = \int_{-\infty}^{\infty} E(\tilde{\nu}) e^{+2\pi i \tilde{\nu} x}\, d\tilde{\nu} \equiv \mathscr{F}^{-1}\{E(\tilde{\nu})\} \tag{3.10}$$

$$E(\tilde{\nu}) = \int_{-\infty}^{\infty} y(x) e^{-2\pi i \tilde{\nu} x} dx \equiv \mathscr{F}\{y(x)\}. \tag{3.11}$$

Equation 3.11 is called the Fourier transform, and equation 3.10 is called the inverse Fourier transform. Two electromagnetic waves, $y_1(x)$ and $y_2(x)$, which are separated by a path difference δ can be given by

$$y_1(x) = \int_{-\infty}^{\infty} E(\tilde{\nu}) e^{2\pi i \tilde{\nu} x}\, d\tilde{\nu}, \tag{3.12}$$

$$y_2(x) = \int_{-\infty}^{\infty} E(\tilde{\nu}) e^{2\pi i \tilde{\nu}(x-\delta)}\, d\tilde{\nu}, \tag{3.13}$$

where x is the amplitude and δ is the optical path difference between the two waves. These equations represent the two waves after recombination at the beamsplitter. By the principle of superposition, the two waves result in

$$y(x) = y_1(x) + y_2(x) = \int_{-\infty}^{\infty} E(\tilde{\nu})[1 + e^{-2\pi i\tilde{\nu}\delta}]e^{2\pi i\tilde{\nu}x}\, d\tilde{\nu}. \tag{3.14}$$

The resultant field $E(\delta, \tilde{\nu})$ is then defined as

$$y(x) \equiv \int_{-\infty}^{\infty} E(\delta, \tilde{\nu})e^{2\pi i\tilde{\nu}x}\, d\tilde{\nu}. \tag{3.15}$$

By comparing 3.14 and 3.15 we find that

$$E(\delta, \tilde{\nu}) = E(\tilde{\nu})[1 + e^{-2\pi i\tilde{\nu}\delta}]. \tag{3.16}$$

The intensity, $B(\delta, \tilde{\nu})$, is

$$B(\delta, \tilde{\nu}) = \tfrac{1}{2}c\epsilon_0 E^*(\delta, \tilde{\nu})E(\delta, \tilde{\nu}), \tag{3.17}$$

where ϵ_0 is the permitivity of free space and c is the velocity of light in vacuum. Substituting $E(\delta, \tilde{\nu})$ from equation 3.16 into the expression for $B(\delta, \tilde{\nu})$ in equation 3.17, and multiplying gives

$$B(\delta, \tilde{\nu}) = c\epsilon_0 E^2[1 + \cos(2\pi\delta\tilde{\nu})]. \tag{3.18}$$

There is no phase relation between the fluxes of different $\tilde{\nu}$ at a given δ from the white light source, so adding the fluxes of different frequency gives

$$I(\delta) \equiv 1/\bar{\tilde{\nu}} \int_0^{\infty} B(\tilde{\nu}, \delta).\, d\tilde{\nu} \tag{3.19}$$

$B(\tilde{\nu}, \delta)$ from equation 3.17 can now be substituted in equation 3.19, and for a white light source $I(\delta)$ becomes

$$I(\delta) = (c\epsilon_0/\bar{\tilde{\nu}})\left\{ \int_0^{\infty} E^2(\tilde{\nu})\, d\tilde{\nu} + \int_0^{\infty} E^2(\tilde{\nu})\cos(2\pi\tilde{\nu}\delta)\, d\tilde{\nu} \right\}. \tag{3.20}$$

If δ is zero this equation becomes

$$\tfrac{1}{2}I(0) = (c\epsilon_0/\bar{\tilde{\nu}}) \int_0^{\infty} E^2(\tilde{\nu})\, d\tilde{\nu}. \tag{3.21}$$

Substituting this into equation 3.20 gives

$$I(\delta) - \tfrac{1}{2}I(0) = \int_0^{\infty} (c\epsilon_0/\bar{\tilde{\nu}})E^2(\tilde{\nu})\cos(2\pi\tilde{\nu}\delta)\, d\tilde{\nu}. \tag{3.22}$$

This equation can be Fourier transformed, giving

$$B(\tilde{\nu}) = (\text{constant}) \int_0^\infty \{[I(\delta) - \tfrac{1}{2} I(0)] e^{(-2\pi i \tilde{\nu} \delta)}\}\, d\delta. \tag{3.23}$$

If the flux versus optical path $I(\delta)$ is a known function of δ for a given wave number, the Fourier transform of $I(\delta) - \frac{1}{2} I(0)$ yields the flux density $B(\tilde{\nu})$ versus wave number $\tilde{\nu}$.

3.5.2 Apodization

The integration limits for the optical path difference in the Fourier analysis are extended to infinity. However, the experimental limits are finite, since the scanner only travels a few cm. Hence, artificial elements are introduced to the spectrum. A truncated integral will show absorbance lines surrounded by sidelobes (feets), rather than the true peak shape. A mathematical modification as a corrective procedure called apodization[1] can be applied to suppress this effect. In this thesis the Blackman-Harris 3-term apodization function was used, as recommended by the instrument manufacturer [98]:

$$f(x) = \sum_{i=1}^{3} a_i \cos\left(\frac{i\pi x}{l}\right) \qquad \text{for } |x| \leq l \tag{3.24}$$

where x is the position and l is total width of window. Coefficients $a_1 = 0.42323$, $a_2 = 0.49755$ and $a_3 = 0.07922$.

3.5.3 FTIR versus dispersive IR spectrometry

The performance of an infrared spectrometer can be determined by measuring its signal-to-noise ratio (SNR). When compared to a dispersive instrument, FTIR has two important advantages that yield higher SNR.

Within a fraction of a second, a FTIR spectrometer samples the entire spectrum with one mirror scan. The spectral range does not affect the time necessary to complete the spectrum. This is known as Fellgett's advantage (Multiplex advantage) [99]. A dispersive instrument requires sampling at individual angles of the monochromator, and hence the time needed for

[1] From greek "a podi" (α φοδι), meaning "no feet".

acquiring a complete spectrum is proportional to the spectral range of interest.

The intensity throughput of a dispersive instrument is limited by the size of the slit, and a high energy resolution requires a narrow slit. In FTIR, there is no need for a slit so higher intensities are possible, and the resolution is only dependent on the mirror travel distance. This advantage is known as the Jacquinot's or the throughput advantage [100].

3.6 Signal to noise ratio

By averaging several hundred scans the random noise in the spectra is reduced since the positive and negative fluctuations in the random noise level cancel out. Assuming random noise, the relationship between the SNR and the number of scans (N) is given as

$$\text{SNR} \propto \sqrt{\text{N}} \tag{3.25}$$

at a given resolution. However, adding spectra indefinitely will not provide a specified SNR. For instance, during measurements there can be some drift in the scanner which contributes to noise that is not random, and the center peak position of the interferogram may shift in a non-random manner.

High resolution spectra are noisier than low resolution spectra. The noise in the interferogram is nearly constant at all points and can represent a significant percentage of the signal in the interferogram wings. Since higher resolution yields longer wings in the interferogram;

$$\text{SNR} \propto \text{Resolution}. \tag{3.26}$$

However, a high resolution spectrum contains more information, and is needed to resolve narrow lines and to observe the true shape of LVMs.

3.7 Instrumentation

The FTIR instrument employed in this thesis is a Bruker IFS 113v spectrometer. The optical set-up is given in figure 3.10, and technical data are listed

in table 3.3. Measurements were mainly performed with a CaF_2 beamsplitter and a InSb detector, to ensure a high signal at wavenumbers in the $2000 - 4000$ cm^{-1} region. In the beginning of the project we measured the samples with a KBr beamsplitter and a DTGS detector to get a broad spectral range overview, and to determine normal vibrational modes.

3.7.1 Details and specifications of the FTIR spectrometer at MiNaLab

The Bruker IFS 113v FTIR spectrometer used in this thesis incorporates an interferometer of Genzel type (instead of the perhaps more commonly known Michelson one). It is initially a design for far-infrared spectroscopy, but still has excellent properties in the mid-infrared region. The optical layout is shown in figure 3.10. Unlike a Michelson interferomter, the light is focused onto the beamsplitter. The beam is reflected and transmitted by the beamsplitter, and pass to two collimating mirrors and then to a double-sided moving mirror (scanner). As the scanner moves, one path length increases and one decreases. For a displacement, x, of the scanner, an optical path difference of $4x$ is generated by the Genzel interferometer. Consequently, the resolution is four times higher compared to a Michelson interferometer with the same optical path difference. However, any tilt on the scanner leads to a doubling in the errors compared to the Michelson design. Small sized beamsplitters also allow more than one to be mounted on a wheel and interchanged without breaking the vacuum in the chamber [101].

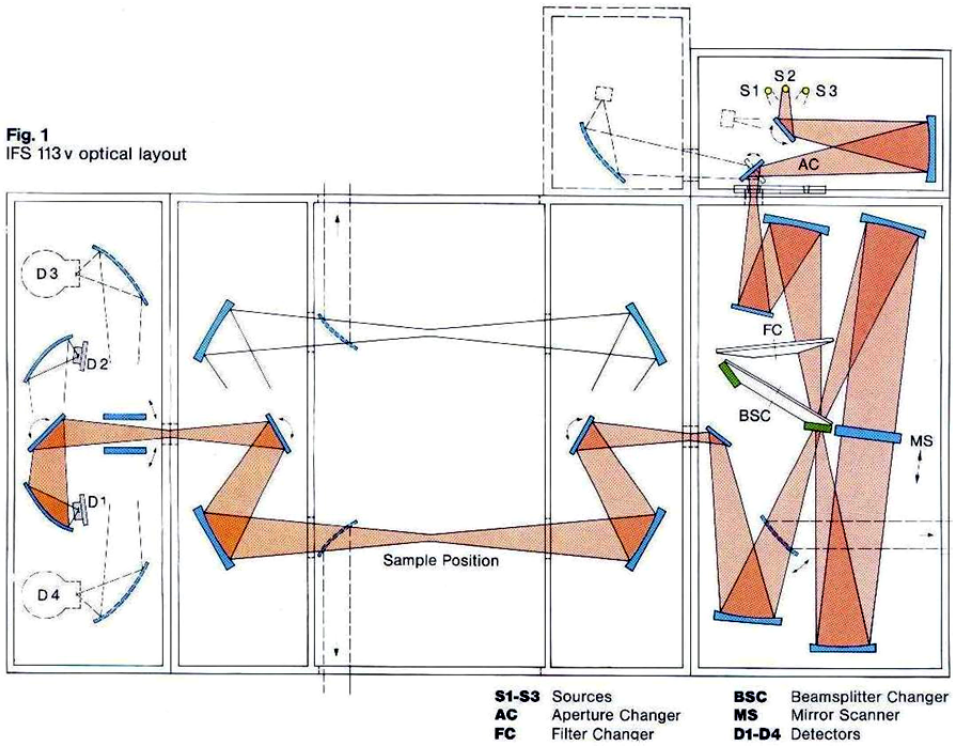

Figure 3.10: Optical layout of the Bruker IFS 113v Genzel spectrometer, copied from the instruments original booklet.

Performance	
Spectral range	$400 - 6000$ cm^{-1} ($0.05 - 0.744$ eV)
Resolution	0.1 cm^{-1}
$\tilde{\nu}$ Accuracy	0.01 cm^{-1}
Base pressure	< 5 mbar
Sample temp	15 or 300 K
Optical system	
IR-Source	SiC Globar ($100 - 6000$ cm^{-1})
Beamsplitters	KBr ($400 - 5200$ cm^{-1})
	CaF_2 ($1250 - 15000$ cm^{-1})
Detectors	DTGS ($350 - 7000$ cm^{-1})
	InSb ($1850 - 10000$ cm^{-1})
Scanner velocity	$0.23 - 3.2$ cm/s
Cryogenic	
Cryostat	Closed Helium CTI-Cryogenics Helix 22 Compressor 8200
Temp Controller	Lake Shore Cryotronics DRC 82C
Data system	
PC	Pentium II Computer, Windows NT, OPUS 2.06 and 3.0.16

Table 3.3: Current set-up and equipment for the Bruker 113v spectrometer at MiNaLab.

Chapter 4

Results and discussion

For sampling the infrared spectra, we have used the OPUS software developed by Bruker Optics. Both sampling and calculation were performed using version 2.16. Baseline correction and smoothing of the spectra were done using version 3.0.16, as kindly provided by Prof. Nielsen at the Chemistry department, UiO. Finally the data was exported to Origin 8E for easy plotting and further evaluation.

4.1 Instrumental configuration

The instrumental set-up was initially configured for studying defects in irradiated silicon, requiring a high signal in the $\sim$1000 cm^{-1} region. A DTGS detector and KBr beamsplitter provide high output in this region (see figure 4.1 and 4.2). We used this configuration to acquire an overview of the absorbance in the mid-infrared region of our samples. However, the signal strength in the $\sim$3300 cm^{-1} region was low and hence, weak hydrogen absorption bands in our thin ZnO samples were barely observable.

Therefore, we mounted a CaF_2 beamsplitter and a InSb detector to gain higher signal in this region. Our versions of the KBr and CaF_2 beamsplitters (BMS) differed somewhat quantatively, from what is illustrated in figure 4.2; using the CaF_2 BMS the signal gain was about 10% at 1800 cm^{-1}, and 25% at 3300 cm^{-1}.

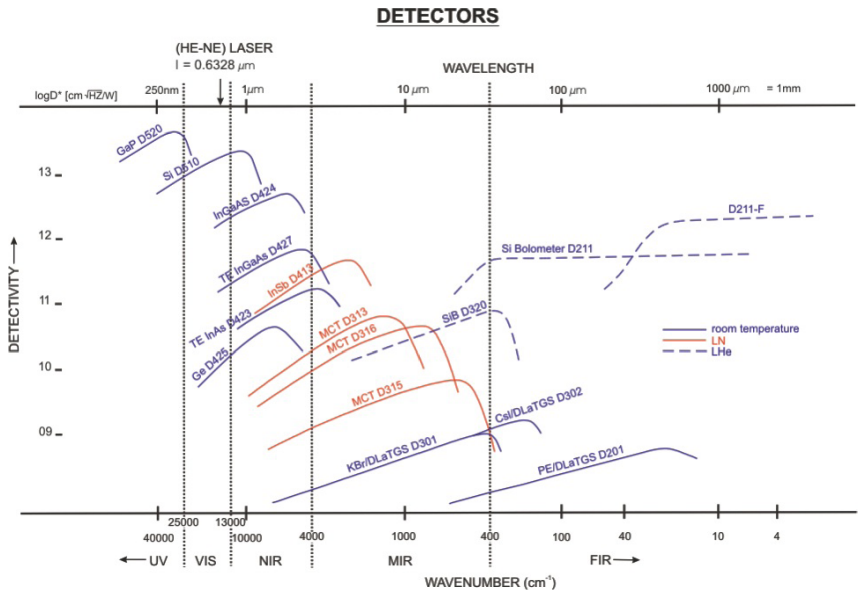

Figure 4.1: Illustration of detector regions and their detectivities. From www.brukeroptics.com.

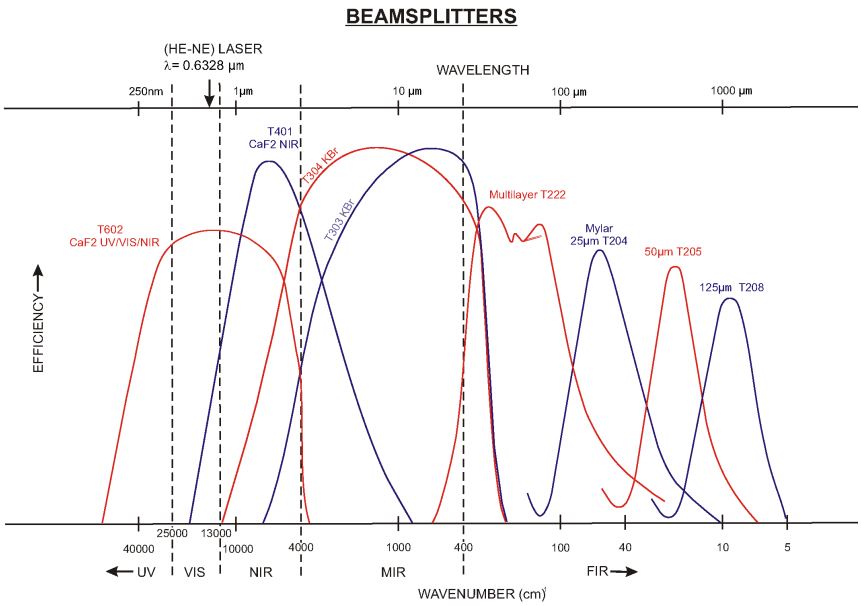

Figure 4.2: Illustration of beamsplitter regions and their efficiencies. From www.brukeroptics.com.

4.1.1 The 100% line

To determine the number of scans that gave the lowest noise level, we measured so called 100% lines for $N = 1$, 4, 16, 32, 64, 256, 512, 1024 and 2048 scans. It was done by ratioing two background spectra acquired under identical conditions of resolution and measurement time, with the second spectrum taken immediately after the first one. A ratio of these spectra indicates how the noise level varies across the spectrum (se figure 4.3).

At high wavenumbers ($\gtrsim$3500 cm^{-1}) there is a significant increase in the noise level, most likely because both vapor absorption in the chamber and the fact that the globar has a lower output at higher wavenumbers.

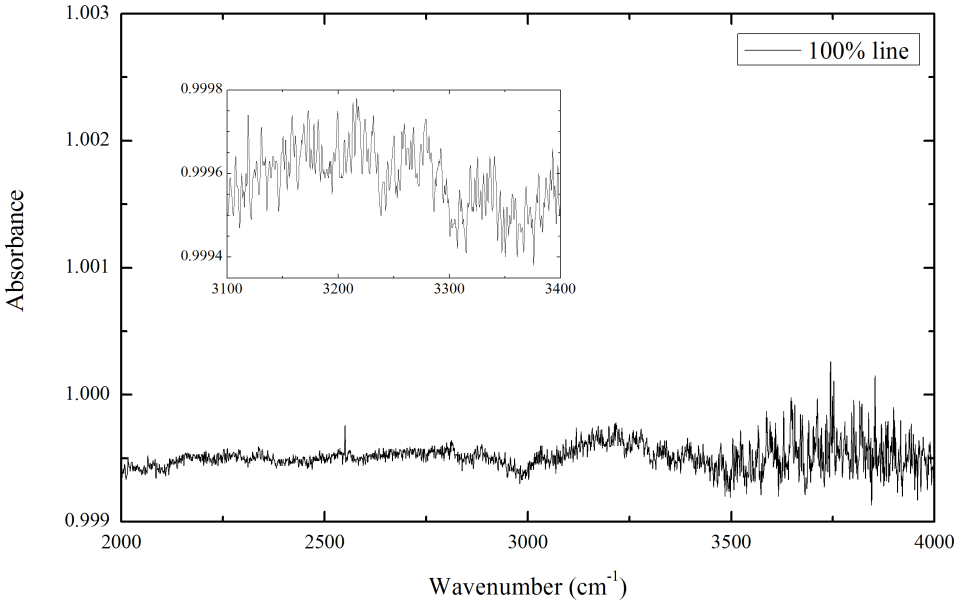

Figure 4.3: A 100% line for 512 scans acquired with CaF_2 beamsplitter, InSb detector and 1 cm^{-1} resolution. The inset shows an expanded view of the $3100 - 3400$ cm^{-1} region.

The root-mean-square values were calculated for two regions, $1900 - 2100$ cm^{-1} and $3200 - 3400$ cm^{-1}. The first region represents the wavenumbers with the highest signal with this instrumental configuration. The second region is where hydrogen-related LVMs are expected. Analyzing these regions provides us with an adequate choice of N for later measurements.

The rms noise is the standard deviation of all the data points the region:

$$x_{\text{rms}} = \sqrt{\frac{1}{n}\sum_{i=1}^{n} x_i^2} \tag{4.1}$$

A plot of the inverse rms values versus the number of scans is given in figure 4.4. The $1900 - 2100$ cm^{-1} region has a significantly lower noise level compared to the $3200 - 3400$ cm^{-1} region, as expected from the region with the highest signal.

According to equation 3.25 the rms noise is proportional to N, which should provide a linear relationship for $N = 1$, 4, 16, 64, 256 and 1024.

As illustrated in figure 4.4 this is not the case for our instrument. The minimum noise level is obtained for 1024 scans in the first region with a rms value equal to 3.4723×10^{-5}. The second region had a minimum noise level for 512 scans with a rms value equal to 8.0948×10^{-5}.

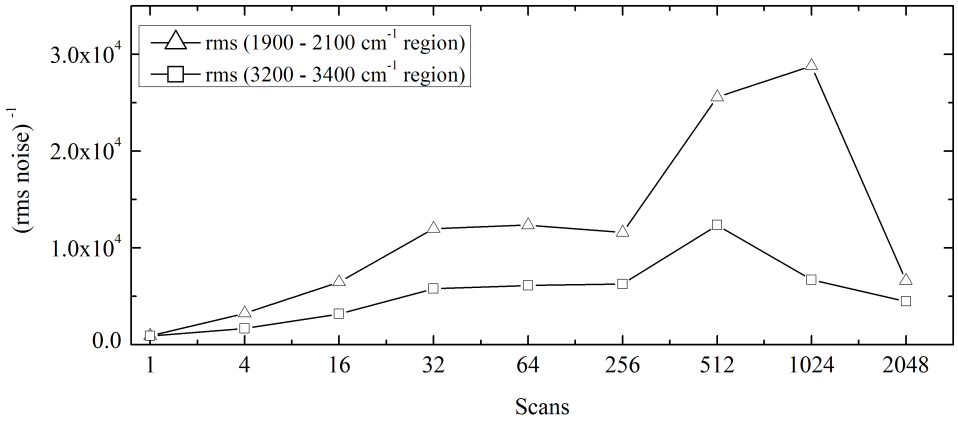

Figure 4.4: Reciprocal of the root-mean-square values versus number of scans for two wavenumber regions.

Under real-time signal controls we observed a shift in the position of the center peak in the interferogram, normally about $1 - 10$ points deviation when checking daily. The scanner is propelled by a linear induction motor and mounted on tracks supported by dual air bearings. Presumably, some drift, related to aperiodic vibrations or vacuum changes, in the mechanics of the scanner is causing the shift. This is a possible reason why a higher noise level occurs when averaging more than 512 scans.

Based on these findings we used 512 scans for later measurements to ensure a high signal to noise ratio in the region of hydrogen-related LVMs.

4.2 IR-spectra obtained with a DTGS-detector

To get an overview of the absorption in the mid-infrared region, the initial configuration with a DTGS-detector and a KBr-beamsplitter was used. As shown in figure 4.5, multiphonon bands are observed at low wavenumbers ($\lesssim$1200 cm^{-1}). These modes are due to vibrations in the lattice causing phonons to interact and induce an electric dipole moment. Several of the bands display high amplitudes revealing strong lattice absorption and lattice reflection in regions below $\sim$1100 cm^{-1}. The observed bands are consistent with previous findings by Collins *et al* [102], Morozova *et al* [103] and Emelie *et al* [104], and have been assigned in table 4.1. An illustration of the atomic displacement patterns causing transverse optical (TO) and longitudinal optical (LO) lattice modes is given in figure 4.6.

The inset in figure 4.5 shows one unassigned LVM at 3336 cm^{-1}. It was the only observable LVM using a DTGS detector with $\mathbf{k}\|c$. No signal was detectable when probing the sample with $\mathbf{k}\perp c$, since the necessary custom made slit, shown in figure 3.3, dramatically reduced the beam size. As a result, the transmitted signal became too low with respect to the response level of the detector.

$\tilde{\nu}$ (cm^{-1})	Assignment
800	2TO(A_1,E_1)
855 - 926	TO(A_1,E_1) + E_2^2, 2 E_2^2
990	LO(A_1,E_1) + TO(A_1,E_1)
1031	LO(A_1,E_1) + E_2^2
1095	2LO(A_1,E_1)

Table 4.1: Assignments of infrared active lattice vibrations observed in as-grown HT ZnO.

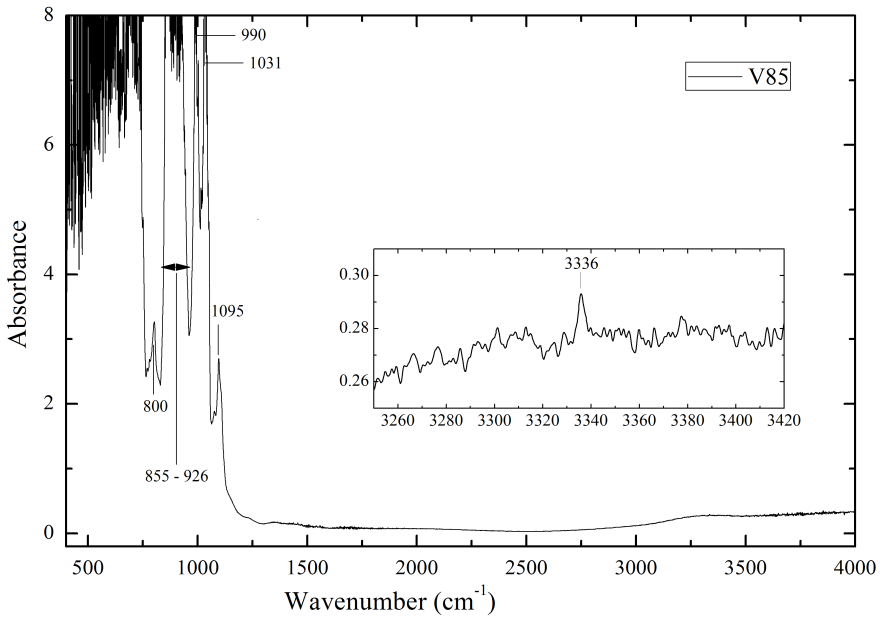

Figure 4.5: Absorption spectrum of as-grown HT ZnO at 15 K. The inset shows an expanded view in the 3300 cm^{-1} region. A LVM at 3336 cm^{-1} is highlighted. The spectrum was acquired with DTGS detector and KBr beamsplitter using unpolarized light $\mathbf{k} \| c$.

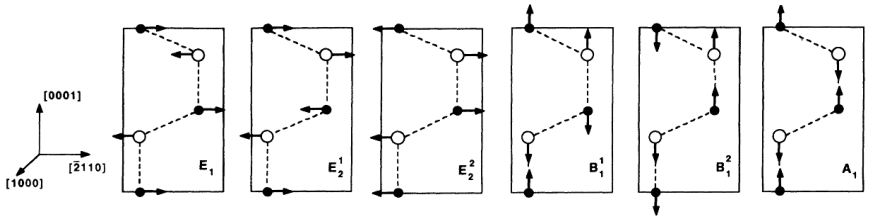

Figure 4.6: Displacement pattern of the optical phonons in a wurtzite crystal structure. From [105].

4.3 SIMS results

Secondary ion mass spectrometry, using a CAMECA IMS 7f micro/nano analyzer at MiNaLab UiO, was employed to measure the deuterium and lithium concentrations versus depth after implantation and annealing. Deuterium is expected to diffuse in a similar way as hydrogen, but the SIMS sensitivity is about three orders of magnitude better for deuterium [106]. First, on the O-face the sample was measured to a depth of ∼20 μm. Then sample beveling was applied aiming to measure concentration profiles in steps along the beveled surface reaching depths of several hundreds of μm. The beveling can be seen in figure 4.7.

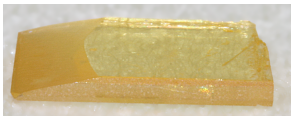

Figure 4.7: A photo showing the beveling of the deuterium implanted sample on the left hand side.

However, it was found difficult to mount the sample in a way that aligned the beveled surface in an optimal direction with respect to the angle of incidence of the primary ions in the SIMS instrument. Hence, another technique had to be used for measuring the concentration at larger depths. We cut off two pieces of the sample and polished away 120 μm and 250 μm, respectively, perpendicular to the *c* axis and measured the concentration at these depths. The result is plotted in figure 4.8. SIMS measurement was also applied on the Zn-face to determine if we had an equal implantation peak and diffusion profile there. Two pieces of the sample were measured, one was polished to a depth of 200 μm (figure 4.9).

On both faces the implantation peak occurred at a depth of ∼2.5 μm below the surface. The annealing has distributed the deuterium into the sample at a concentration level of 2.2×10^{17} cm^{-3}, detected to a depth extending to >122 μm on the O-face. However, for depths of $\sim200-250$μm no in-diffusion of deuterium is detected.

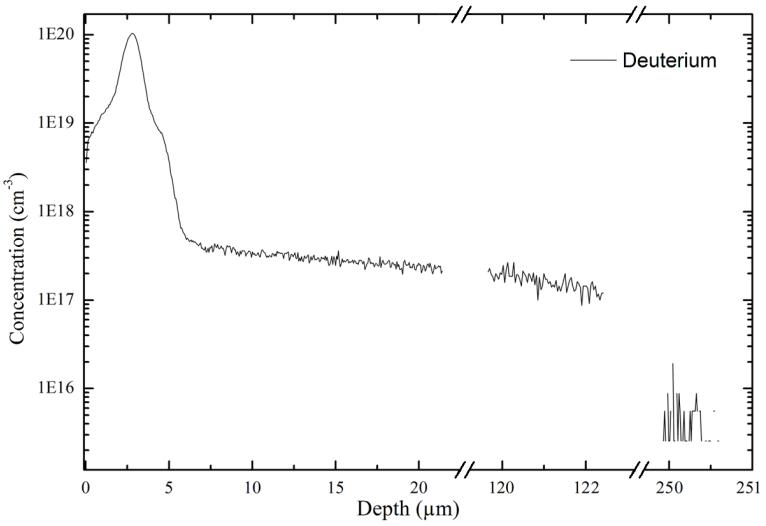

Figure 4.8: O-face SIMS measurement of the concentration of deuterium in sample V92 after implantation and annealing for 70 hours at 400°C.

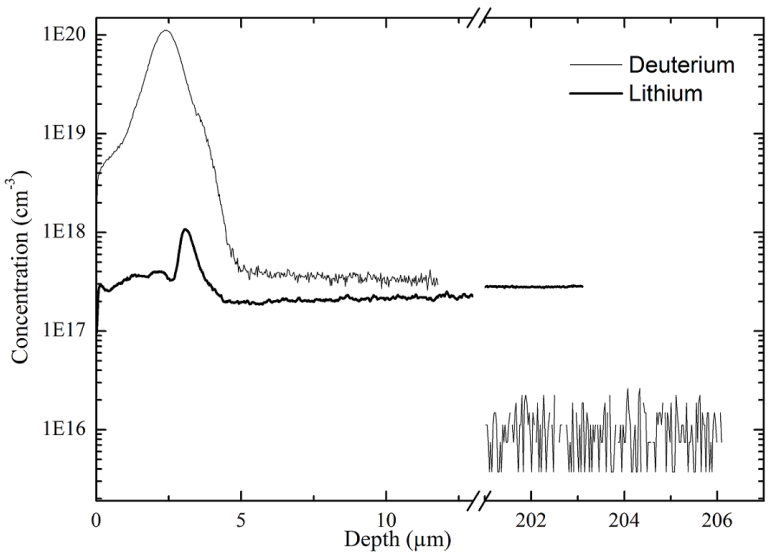

Figure 4.9: Zn-face SIMS measurement of the concentration of deuterium and lithium in sample V92 after implantation and annealing for 70 hours at 400°C.

Lithium atoms have accumulated inside the deuterium implantation region to a peak concentration of 1.1×10^{18} cm^{-3}. This is presumably related to the generation of defects during ion implantation. TRIM [107, 108] calculations predict approximately twice as many zinc vacancies compared to oxygen vacancies. Zinc vacancies are known from positron annihilation spectroscopy studies [37] to act as strong traps for migrating Li species and this trapping is most likely responsible for the observed Li in the implantation region. Below the implanted region, the Li concentration is rather uniformly distributed and throughout the bulk of the sample a concentration of 3×10^{17} cm^{-3} is revealed.

The diffusion profile for deuterium does not have a typical shape as expected for a semi-infinite source model [93]. As reported by Johansen *et al* [106], we assume a similar trap limited diffusion model for deuterium and hydrogen migration in our ZnO samples. The concentration of trapping sites for deuterium was reported to be close to the concentration of lithium, and a similar behaviour is also observed in our samples. Hence, it is tempting to suggest that deuterium is trapped by lithium or by lithium-related complexes.

4.4 Results from resistivity measurements

The resistivity was measured with a four point probe set-up for all the samples in as-grown state and after annealing. The probe tips where dipped in eutectic InGa to improve contact to the samples. All the as-grown samples displayed resistivities >10-100 kΩcm, which is above the operational range of the set-up for a more accurate determination. The resistivity of the deuterium and hydrogen implanted samples decreased to 1.06 ± 0.18 Ωcm (both faces) and to 2457.1 ± 611.3 Ωcm (O-face), respectively (see table A.1 in appendix A), when measuring after the layer containing the implantation peak had been removed. The Zn-face of the hydrogen implanted sample had too high resistivity for our set-up, indicating a resistivity >10 kΩcm. At least two questions arise from the results in table A.1. Why is the resistivity so much higher on the H-implanted sample (V91), and why is the resistivity different on the two faces of the sample? The answer to the

former question could be due to a higher concentration of hydrogen in the as-grown V92 sample, compared to the as-grown V91 sample, as will be discussed later. The answer to the second question is not fully known but the samples are highly compensated and a very small variation in the net concentration of free electrons between the O-face and Zn-face can easily account for the observed difference in resistivity.

To quantify the net carrier concentration in the samples equation 3.2 is applied with negligible contribution from hole since the samples are of n-type:

$$\frac{1}{\rho} = q\mu_n n, \tag{4.2}$$

which gives a net carrier concentration of $(6.0 \pm 1.0) \times 10^{16}\text{cm}^{-3}$ for the deuterium implanted sample, and $(2.7 \pm 0.6) \times 10^{13}\text{cm}^{-3}$ for the hydrogen implanted sample if we assume a mobility of 100 cm^2/Vs at RT [109].

4.5 Absorbance spectra aquired using DTGS detector

Using the DTGS detector and the KBr beamsplitter all the absorbance spectra were recorded with the propagation of the IR light parallel to the c axis of the crystal. However, in this configuration of the FTIR spectrometer there was a low signal in the region of characteristic O-H modes, and hence the absorption spectra were very noisy. Despite the noise, a weak LVM at 3336 cm^{-1} was observed in two of the samples (figure 4.10) and this band will be further discussed in the following paragraph using a more appropriate configuration of the FTIR spectrometer, with respect to the wavenumber range valid for characteristic O-H modes.

4.6 Absorbance spectra aquired using InSb detector

To gain a higher signal in the wavenumber region above $\sim$2000 cm^{-1}, we mounted the CaF_2 beamsplitter and the liquid nitrogen cooled InSb detector. For all the samples, the signal to noise ratio is significantly higher using this detector compared to that for the DTGS detector. However, at wavenumbers above $\sim$3450 cm^{-1} a noisy region occurs occasionally, likely

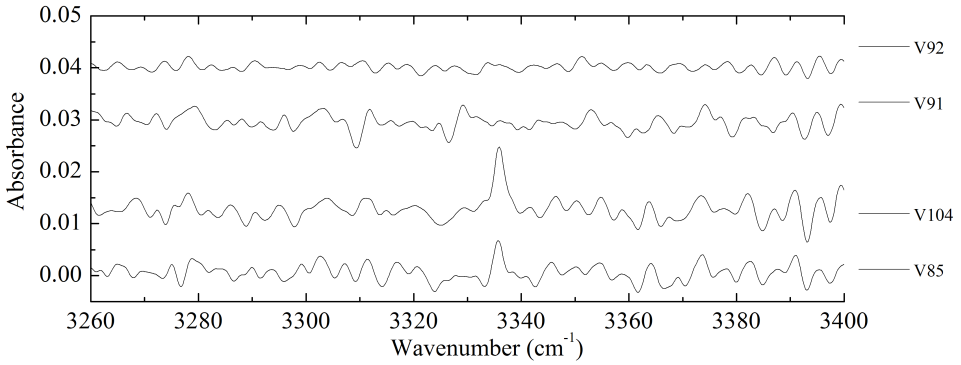

Figure 4.10: Absorption spectra of as-grown HT ZnO measured at 15 K with unpolarized light $\mathbf{k}||c$ using DTGS detector and KBr beamsplitter. Spectra are offset vertically for clarity.

caused by interference related to internal reflection from the sample surfaces. Another contributing effect can be variation in the amount of vapor in the instrument chamber when measuring the background spectra and the sample spectra. Spectra of the as-grown samples (V85 and V104) were acquired before and after annealing to determine any change in the LVMs caused by the annealing alone. The spectra of the hydrogen and deuterium implanted samples were acquired after implantation and after annealing, and finally after removal of the implantation region by polishing. Spectra recorded with IR light parallel and perpendicular to the *c* axis of the crystal are depicted in figures 4.11 and 4.12, respectively. Tables 4.2 and 4.3 give integrated absorbance for all the observed peaks.

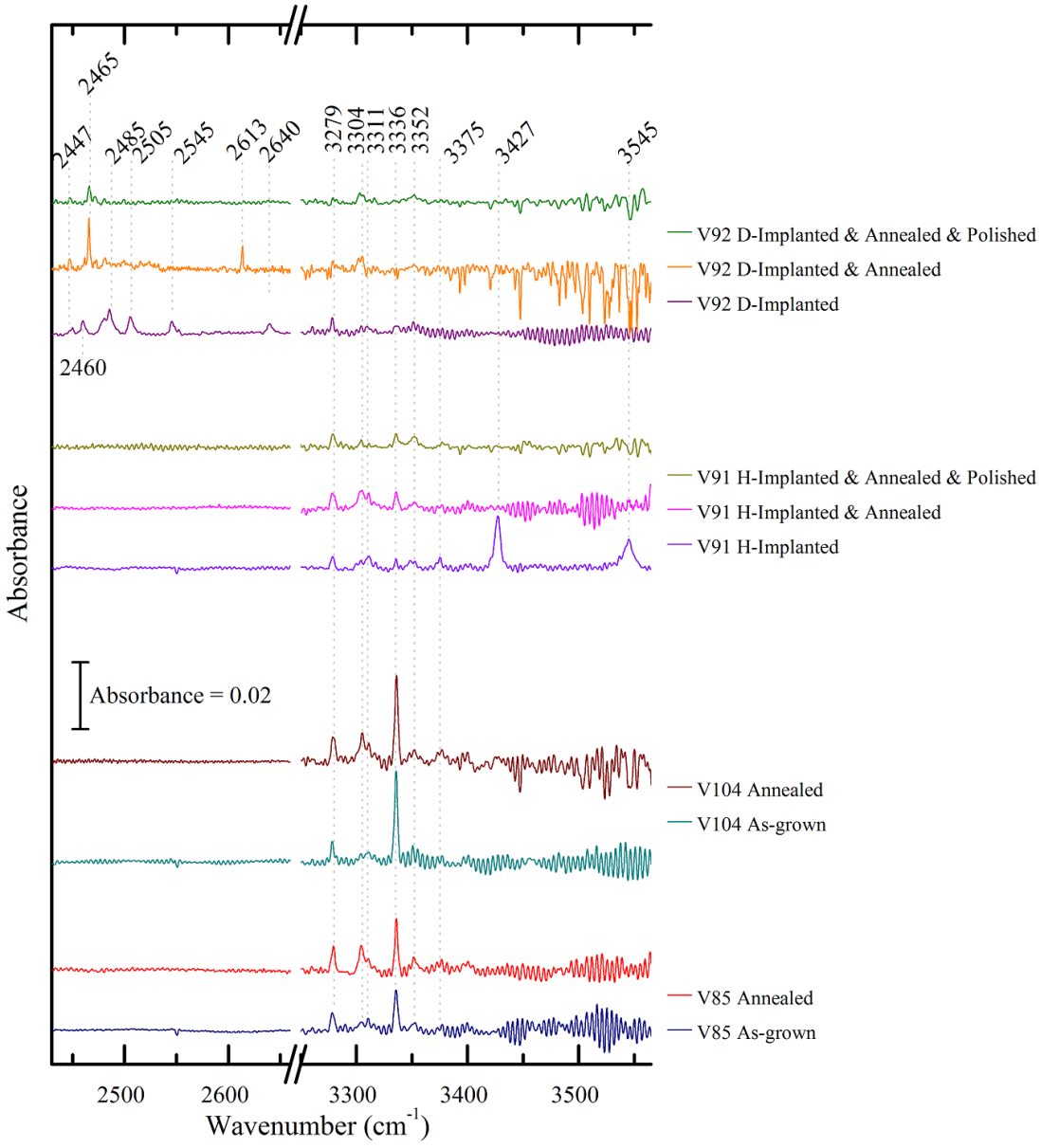

Figure 4.11: Absorption spectra of HT ZnO measured at 15 K with unpolarized light $\mathbf{k} \| c$ using InSb detector and CaF_2 beamsplitter. Spectra are offset vertically for clarity.

Sample, Peak:	2447	2460	2465	2485	2505	2545	2613	2640
V92 Implanted		0.0073		0.0324	0.0109	0.0061		0.0078
V92 Annealed	0.0032		0.0160				0.0071	
V92 Polished	0.0018		0.0052					

Sample, Peak:	3279	3304	3336	3352	3375	3427	3545
V85 As-grown	0.0108	0.0044	0.0245	0.0101			
V85 Annealed	0.0126	0.0182	0.0290	0.0139			
V104 As-grown	0.0091	0.0018	0.0477				
V104 Annealed	0.0153	0.0151	0.0483	0.0030	0.0054		
V91 Implanted	0.0065	0.0065	0.0025	0.0009	0.0069	0.0521	0.0363
V91 Annealed	0.0105	0.0131	0.0094	0.0020			
V91 Polished	0.0080	0.0041	0.0063	0.0025			
V92 Implanted	0.0051						
V92 Annealed		0.0230					
V92 Polished	0.0045	0.0033					

Table 4.2: Integrated absorbance, IA, (cm^{-2}) for the observed peaks in figure 4.11. The peaks at 3304 and 3311 cm^{-2} overlap; the latter has not been integrated, and the IA for the 3304 peak is only an approximation.

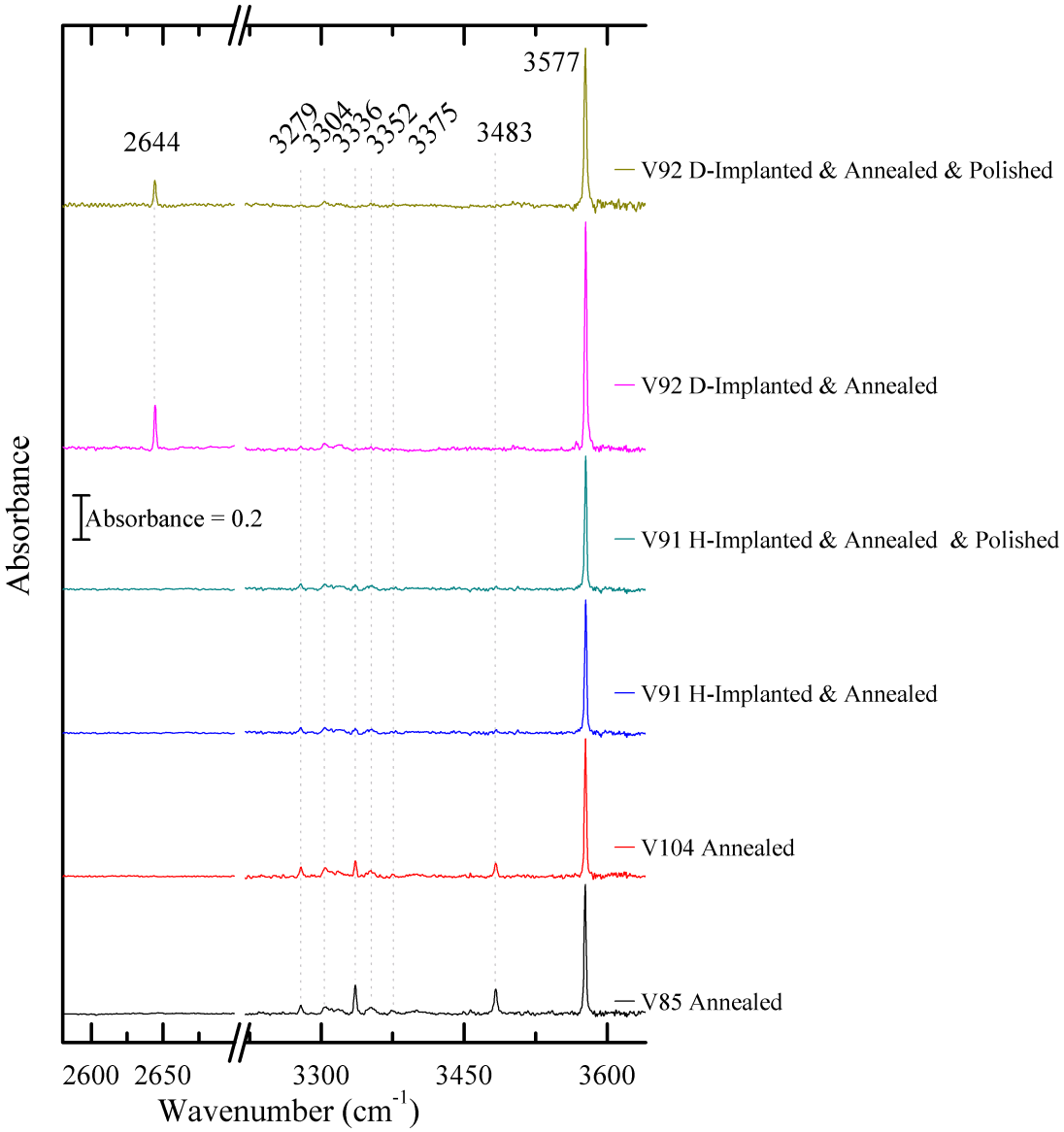

Figure 4.12: Absorption spectra of HT ZnO measured at 15 K. All the samples had a thickness of 1 cm, except V92 (0.6 cm). The absorbance for V92 is corrected by a factor $\frac{10}{6}$. Unpolarized light with $\mathbf{k} \perp c$ was used. Spectra are offset vertically for clarity.

Sample, Peak:	2644	3279	3304	3336	3352	3484	3577
V85 Annealed		0.1134	0.1480	0.3738	0.0235	0.3664	1.4963
V104 Annealed		0.1215	0.1707	0.1955	0.0415	0.2165	1.5611
V91 Annealed		0.0611	0.0720	0.0899		0.0162	1.58187
V91 Polished		0.0403	0.0545	0.0659		0.0267	1.5086
V92 Annealed	0.3697	0.0350	0.0815				2.8817
V92 Polished	0.2330		0.0055				2.1588

Table 4.3: Integrated absorbance (cm^{-2}) for the observed peaks in figure 4.12.

4.6.1 As-grown samples, V85 and V104

Using the InSb detector, absorption peaks at 3279, 3304, 3352 and 3375 cm^{-1} emerge, together with the previously mentioned one at 3336 cm^{-1} in the as-grown samples for $\mathbf{k}\|c$. Two strong additional peaks at 3483 and 3577 cm^{-1} are seen for $\mathbf{k}\perp c$. All these peaks appear in the region of characteristic O-H stretch modes. The peak at 3577 cm^{-1} is dominant and the position is in very good agreement with the approximation (3578.14 cm^{-1}) made in section 2.4.5.2 for the O-H stretching mode using the Morse potential. The position is also close to the experimental value of 3555.6 cm^{-1} reported for a free OH^- [110]. The theoretically predicted wavenumbers given in table 2.3 (page 25) are also fully consistent with the conclusion that the observed peaks are due to O-H bonds. Furthermore, compared to the later discussed O-D peaks, we observe a good agreement in the isotopic shifts as listed in table 4.4.

After annealing, all the four absorption peaks observed with $\mathbf{k}\|c$ increase in strength. A similar behaviour has previously been observed by Shi *et al* [111], where a O-H stretching line (in vapor phase ZnO) at 3326.3 cm^{-1} grew in intensity after annealing at $\geqslant$400°C, in the absence of an external source of hydrogen. However, their peak was not detected before annealing, implying that an IR inactive hydrogen configuration is present in as-grown ZnO. An interstitial H_2 molecule was proposed as a likely candidate. Recently, Karazhanov and Ulyashin [112] reported an H_2^* complex where one of the H atoms is tightly bonded to O and the other H forms

O-H peaks	O-D peaks	Ratio, $\tilde{\nu}_H/\tilde{\nu}_D$	Comment
3577	2644	1.353	Both $\tilde{\nu}$ stable, ($\mathbf{k}\perp c$)
3545	2640	1.343	Implantation related
3483	-	-	Stable, no corresponding $\tilde{\nu}_D$
3427	2545	1.347	Implantation related
3375	2505	1.347	$\tilde{\nu}_D$ disappears after annealing
3352	2485	1.349	$\tilde{\nu}_D$ disappears after annealing
3336	2465	1.353	Both $\tilde{\nu}$ stable, ($\mathbf{k}\|c$)
3311	2460	1.346	$\tilde{\nu}_D$ disappears after annealing
3304	2447	1.350	$\tilde{\nu}_D$ disappears after annealing
3279	-	-	Stable, no corresponding $\tilde{\nu}_D$
-	2613	-	$\tilde{\nu}_D$ disappears after annealing and no corresponding $\tilde{\nu}_H$

Table 4.4: Isotopic shifts calculated from the H-implanted and D-implanted samples.

a chemical bond with the nearest Zn. Compared to the H-H bond, this complex was found to be more stable when the Fermi level position moves close to the conduction-band minimum i.e., in highly *n*-doped samples. The 3326.3 cm^{-1} band is not found in our samples but the general trend of increasing peak intensities after annealing may be related to an effect of the type discussed in [112].

4.6.2 Hydrogen implanted sample, V91

The hydrogen as-implanted sample has two new strong absorption peaks at 3427 and 3545 cm^{-1} ($\mathbf{k}\|c$). The as-grown spectrum from this sample is acquired with a DTGS detector, as shown in figure 4.10, but the 3336 cm^{-1} line is substantially weaker after implantation and then recovers by annealing. After annealing, we observe an increase also in the absorbance of the 3279, 3304, and 3352 cm^{-1} lines, while the two dominant peaks at 3427 and 3545 cm^{-1} disappear. Most likely, the 3427 and 3545 cm^{-1} lines are related to O-H complexes linked to implantation induced defects like V_{Zn}, V_O, Zn_i, O_i, as they are expected to annhilate upon moderate annealing.

The centers Zn_i, V_{Zn} and V_O have been suggested to anneal out at $\leqslant$600 K [113, 114, 115], in accordance with theory caluclations [39, 116, 117], while O_i is believed to be even more mobile than the vacancies. Such defect annihilation processes contribute to a rapid recovery of irradiation-induced defects in ZnO by annealing and render the material radiation hard [118]. As our annealed samples were heat treated at 400°C, a significant amount of the intrinsic defects will anneal out causing the lines at 3427 and 3545 cm^{-1} to disappear.

Furthermore, the 3427 and 3545 cm^{-1} lines were only observed in the hydrogen as-implanted sample, and not in the deuterium as-implanted one, which is expected to contain similar implantation-induced defects, supporting the assignment to O-H containing complexes.

After the implantation peak was removed by polishing, the IR spectrum showed a minor decrease in the 3304 and the 3336 cm^{-1} lines, in contrast to the 3279 and 3352 cm^{-1} lines. This may indicate an enhancement in the surface region for the two former lines, as the decrease was not proportional to the thickness reduction but more pronounced.

A main question is why the intentional introduction of hydrogen did not increase the absorbance peaks significantly compared to the as-grown samples, as expected in the initial stage of this project. Could our implanted hydrogen dose be too small compared to the amount of hydrogen already present in the as-grown state? Did the implanted hydrogen reside at IR inactive configurations, e.g. molecular H_2? This is further discussed in paragraph 4.7.

4.6.3 Deuterium implanted sample, V92

The as-implanted deuterium sample has an absorption peak at 3279 cm^{-1}, which also exists in the hydrogen sample, and as previously seen in the DTGS measurement there are no distinct lines in the 3300 cm^{-1} -region. At lower wavenumbers, where we expect O-D modes, five new peaks at 2447, 2460, 2485, 2505, 2545 and 2640 cm^{-1} occur. As shown in table 4.4, these modes most certainly have a relation to the peaks observed in the hydrogen sample. The two dominant 3427 and 3545 cm^{-1} O-H lines have two

D-implanted isotopic companions at 2545 and 2640 cm^{-1}, with $r = 1.347$ and $r = 1.343$, respectively. The intense and stable peaks at 2644 and 3577 cm^{-1} ($\mathbf{k} \perp c$) has a $r = 1.353$. These r values provide almost unambiguous evidence for O-D and O-H bonds in the samples, presumably linked to different defect configurations. The 2613 cm^{-1} band which is rather pronounced after annealing, does not have any distinct companion in the H-spectra. If it is a O-D mode one would expect a O-H counterpart at ≈3527 cm^{-1}, but no lines are observed in this region. However, that is a noisy region disturbed by water vapor absorption, but a weak line of substantial amplitude should still be resolved. The line persisted during the annealing, but disappeared after the polishing. This indicates that the line is due to a O-D configuration linked to an implantation-induced defect which is more strongly generated by D ions than H ions.

After annealing, only the 2447, 2465 and 2644 cm^{-1} bands remained and as seen in table 4.4, these modes have isotopic counterparts in good agreement with the stable 3304, 3336 and 3577 cm^{-1} modes in the as-grown samples.

4.7 Quantification of the hydrogen content

From the SIMS measurements one can integrate the diffused amount of deuterium in the sample, and relate that to the absorption strength per vibrating hydrogen species, ξ (cm). Assuming uniform distribution, the integrated absorbance of an absorption peak is related to the absorbant concentration, N, by

$$N = \frac{\int \alpha(\tilde{\nu})}{\xi} \, d\tilde{\nu} \tag{4.3}$$

where α is the absorption coefficient related to the absorbance, A, by $\alpha = A/l$, where l is the sample thickness. The penetration depth of the $\sim 10^{17}$ cm^{-3} deuterium level cannot be precisely determined. From the SIMS measurement, figures 4.8 and 4.9, we only know it is between 122 and 250 μm on the O-face and <200 μm on the Zn-face. For simplicity and most likely also very realistic, a similar diffusion depth on both faces between 122 and 200 μm is assumed. The deuterium dose in the polished sample

becomes then $(1.46 \pm 0.54) \times 10^{17}\text{cm}^{-2}$. The integrated absorbance for the O-D peak at 2644 cm^{-1} equals 0.233 cm^{-2}, and by applying equation 4.3, the absorbance strength per D becomes $\xi_D = (1.72 \pm 0.63) \times 10^{-18}$ cm. A similar treatment can in principle be made for hydrogen but the detection limit for H in ZnO by SIMS is in the mid 10^{17} cm^{-3} range and integration of the concentration-versus-depth profiles is not meaningful. On the other hand, to determine the absorbance strength per H species a conversion factor is needed but to our knowledge there is no value reported in the literature for H in ZnO. However, as a first approximation an average of factors known from other oxides i.e. $LiNbO_3$ (= 1.31) and TiO_2 (= 1.88) [119, 120] is used. This provides us with an $\xi_H = (2.74 \pm 1.01) \times 10^{-18}$ cm, which is close to the approximation by McCluskey *et al* ($\sim 2 \times 10^{-18}$) for the hydrogen 3326 cm^{-1} mode [80].

Applying this value of ξ_H, which seems rather reasonable compared with that of ξ_D, the hydrogen concentration in the samples can be estimated by determining the integrated absorbance of the dominant 3577 cm^{-1} modes. The estimated concentration values are given in table 4.5.

A relatively large concentration of hydrogen is deduced for all the investigated samples. For instance in the deuterium implanted sample, V92, the hydrogen concentration is about a factor three higher than the lithium concentration.

Similar considerations for the $\mathbf{k}\|c$ measurements in figure 4.11 is a bit more complicated for several reasons. First, the 2465 cm^{-1} O-D related peak is weak compared to the noise level, and the isotopic shift is uncertain. Both the 3336 and 3304 cm^{-1} bands are likely hydrogen substitution modes and these modes are also weak with respect to the noise level. In addition,

Sample	H-concentration (cm^{-3})
V85	$(5.87 \pm 2.17) \times 10^{17}\text{cm}^{-3}$
V104	$(6.13 \pm 2.26) \times 10^{17}\text{cm}^{-3}$
V91	$(5.92 \pm 2.19) \times 10^{17}\text{cm}^{-3}$
V92	$(8.44 \pm 3.12) \times 10^{17}\text{cm}^{-3}$

Table 4.5: Hydrogen concentration estimated from the 3577 cm^{-1} line.

the thickness of the manually polished V92 sample may suffer from a rough surface.

From the data given in table 4.5 we can conclude that the implanted hydrogen dose (in total $4 \times 10^{16}\text{cm}^{-2}$) is close to the dose already present in the as-grown sample ($2.8 \pm 1.0 \times 10^{16}\text{cm}^{-2}$). This could indeed explain why the resistivity did not exhibit a large decrease, and why that the hydrogen peaks in the IR spectra were not significantly enhanced by the hydrogen implantation. The 5% reduction in the integrated absorbance of the 3577 cm^{-1} peak correlate perfectly with the 5% reduction in sample volume after polishing.

One open question regarding the deuterium implanted sample, is why the integrated absorbance of the 2644 cm^{-1} peak reduced 37% and the 3577 cm^{-1} peak reduced 25% compared to the 5% polishing of the sample. This indicates strongly that both these vibrational modes are promoted in the implantation region, containing a high local concentration of defects. This holds especially for the D implant which generate about a factor of two higher defect concentration than the H implants used, according to TRIM calculations.

4.8 Possible defect identification

Recent reports have assigned the 2644/3577 cm^{-1} peaks to OD-Li/OH-Li centers, with the O-H bond arranged parallel to the *c* axis (figure 4.13) [86, 87]. An analogous OH-Li defect has even been reported in MgO crystals [121, 122].

Our measurements support a parallel to the *c* axis configuration for these bands. Further, the SIMS results in figure 4.9 show a difference between the Li and D concentrations of less than a factor of two, i.e., they exhibit concentrations of the same order of magnitude suggesting that Li is a strong trap for migrating D/H-species in accordance with findings from other semiconductors [123].

In addition, we observe a series of other peaks, which are detectable both parallel and perpendicular to the *c* axis, but without further investigations it is not possible to suggest any specific configurations. However, the

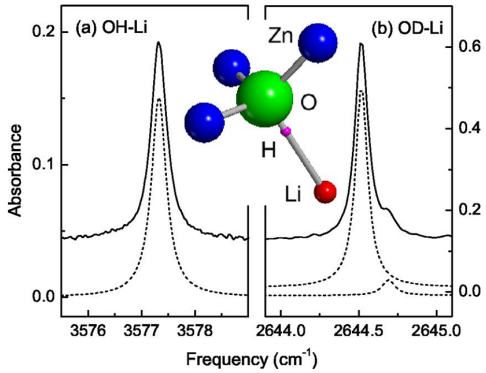

Figure 4.13: A suggested configuration of an OH-Li complex. From [87].

close isotopic ratio between several of the band positions in the H- and D-implanted samples may suggest that vacancies are closely linked to these O-H (O-D) configurations.

The 3484 cm^{-1} peak was the only one not to be observed in the implanted samples. To the best of our knowledge the peak has not been assigned in the literature, however a O-H bond aligned parallel to the *c* axis stands out as a likely candidate.

Chapter 5

Summary

5.1 Conclusions

Absorbance spectra of single crystalline HT ZnO samples have been recorded with IR light both parallel and perpendicular to the *c* axis of the samples by employing FTIR. Eight vibrational O-H modes with excellent isotopic shifts have been observed, in addition to three modes at 2613, 3279 and 3483 cm^{-1} with no isotopic companion. We observed several previously unreported O-D modes related to the implantation region and it is speculated that many of the O-H (O-D) modes are close associated with defect structures involving vacancies.

The infrared absorption strength per deuterium species has been determined to $\xi_D = (1.72 \pm 0.63) \times 10^{-18}$ cm for $\mathbf{k} \perp c$ measurements, based on controlled deuterium introduction into as-grown hydrothermal ZnO, and correlation between FTIR and SIMS. Based on results from other oxides, the absorption strength per hydrogen species in ZnO is estimated to $\xi_H = (2.74 \pm 1.01) \times 10^{-18}$ cm.

The as-grown hydrogen content in the samples has been deduced to be of the same order of magnitude compared to the implanted dose. This could explain why the hydrogen peaks in the IR spectra were not significantly enhanced by the hydrogen implantation. The total concentration of hydrogen in the investigated samples was two orders of magnitude larger compared to the solubility of hydrogen in ZnO strongly suggesting that

a large fraction of the H atoms are trapped by defects/impurities. For instance, our results support a parallel to *c* axis configuration for a Li-complex which is anticipated to be a strong trap for migrating H/D species.

Annealing of the ZnO samples provided an increase in the absorption strength, which may indicate an activation of diatomic hydrogen (not IR active) present in the as-grown state.

5.2 Suggestions for future work

The ξ_H factor could be determined with more accuracy by implantation of a higher dose of hydrogen, to ensure a more significant increase in the hydrogen content.

The annealing process could be extended beyond 70 hours at 400°C to ensure an even deeper diffusion length and more homogeneous distribution throughout the sample.

On the technical side, it would be interesting to do some modifications to determine the nature of the observed bands. A polarizing filter could precisely determine the polarization dependence and the angle of the bonds with respect to the *c* axis.

The uni-axial stress dependence could be measured by mounting the samples in a diamond-anvil cell. This could help determine the structure and symmetry of the defects, as Limpijumnong and Zhang [124] predicted a different behaviour of the O-H bonds in the AB and BC locations.

Investigations of the absorption bands as a function of annealing time and temperature could reveal if the activated hydrogen species decayed and formed IR inactive H_2 species.

Appendix A

Resistivity measurements

	V91 O-face			V92 Zn-face			V92 O-face		
Nr.	V (mV)	I (μA)	ρ (Ωcm)	V (mV)	I (mA)	ρ (Ωcm)	V (mV)	I (mA)	ρ (Ωcm)
1	20.5	2.7	2269.3	10.0	2.2	1.4	10.0	2.6	1.1
2	30.0	4.1	2186.9	15.0	3.3	1.4	23.0	6.0	1.1
3	50.0	6.8	2197.7	40.0	8.5	1.4	50.0	13.0	1.1
4	20.2	2.1	2875.0	9.3	2.8	1.0	10.0	3.8	0.8
5	30.1	2.9	3102.2	30.0	8.7	1.0	25.0	9.6	0.8
6	50.8	4.2	3615.0	50.0	14.3	1.4	50.0	18.3	0.8
7	15.0	2.0	2242.6	10.0	2.8	1.1	10.0	3.0	1.0
8	20.0	3.2	1868.0	24.0	7.0	1.0	18.0	5.5	1.0
9	50.0	8.5	1758.1	50.0	14.4	1.0	50.0	14.2	1.1

Table A.1: Electrical measurements acquired on both faces of sample V92 and on the O-face of sample V91. The sample V91 has been implanted with H, annealed at 400°C for 70 h and then polished to a depth of ∼15 μm on both faces. The same treatment holds for the sample V92 except using implantation with D and not H.

Appendix B

Wet chemical etching of ZnO

A side project was to investigate a reported isotropic ZnO etch for removal of the thin region containing the implantation region.

B.1 Wet chemical etching of ZnO

The wet etch was based on a patent describing an polish etch for HT ZnO [125]. The mixture was a 0.2 mol/L ethylenediaminetetraacetic acid disodium dihydrogen (EDTA solution) and 99% ethylenediamine (ED) with volume ratio of 20:1. A drop of positive photoresist (Rohm Haas S1813) was deposited on two samples, so an etch step later could be observed in a SEM, and measured with a stylus profilometer. The SEM picture of the O-face is given in figure B.1, and the picture of the Zn-face in figure B.2.

After 7 hours of etching, we measured the etch rate to 16.0 ± 1.5 µm/hour on the O-face, and 0.7 ± 0.1 µm/hour on the Zn-face. As seen on the SEM pictures, the etch solution is not suitable for removal of thick layers, as it generates a significant amount of etch pits.

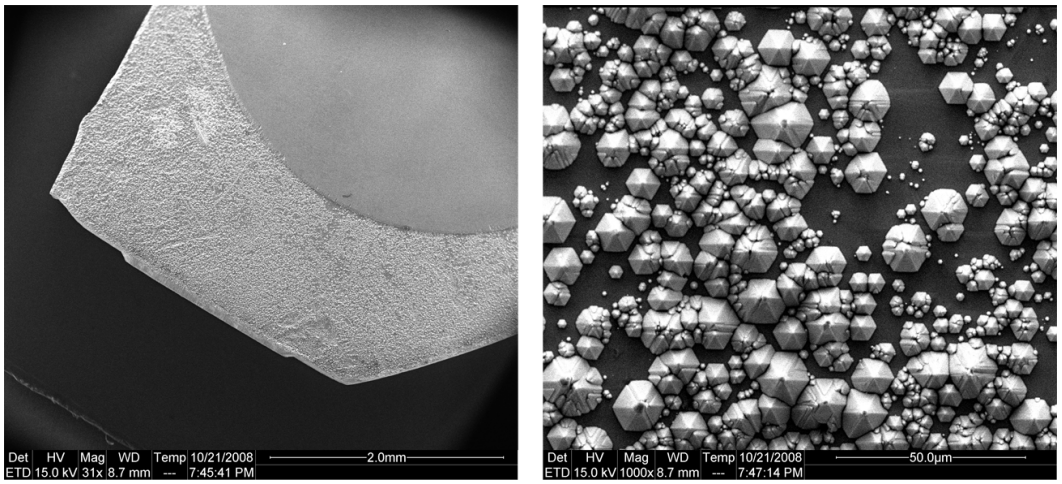

Figure B.1: SEM picture of the O-face of etched ZnO surface. The flat surface on top (picture on left hand side) was covered with photo-resist during etching.

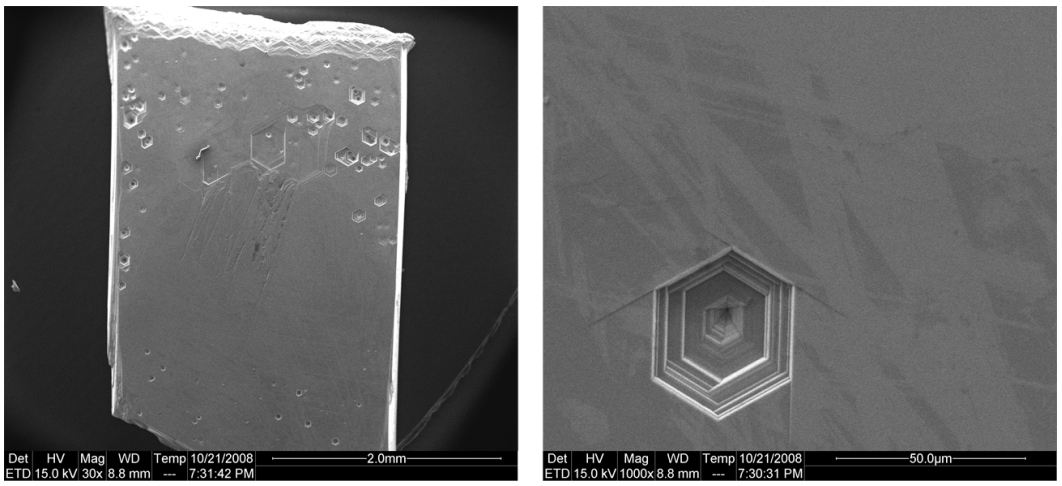

Figure B.2: SEM picture of the Zn-face of etched ZnO surface. The flat surface in the centre (picture on left hand side) was covered with photo-resist during etching.

References

[1] C Klingshirn. ZnO: From basics towards applications. *Physica Status Solidi (b)*, 244(9):3027, 2007.

[2] DG Thomas and JJ Lander. Hydrogen as a Donor in Zinc Oxide. *The Journal of Chemical Physics*, 25:1136, 1956.

[3] WL Bragg. The crystalline structure of zinc oxide. *Philosophical Magazine*, 39(5):647–651, 1920.

[4] RJD Tilley. *Crystals and Crystal Structures*. John Wiley & Sons, 2006.

[5] R Triboulet, V Munoz-Sanjosé, R Tena-Zaera, MC Martinez-Tomas, and S Hassani. THE SCOPE OF ZINC OXIDE BULK GROWTH. *Zinc Oxide-a Material for Micro-and Optoelectronic Applications*, 2005.

[6] DC Reynolds, CW Litton, DC Look, JE Hoelscher, B Claflin, TC Collins, J Nause, and B Nemeth. High-quality, melt-grown ZnO single crystals. *Journal of Applied Physics*, 95:4802, 2004.

[7] DC Look, DC Reynolds, JR Sizelove, RL Jones, CW Litton, G Cantwell, and WC Harsch. Electrical properties of bulk ZnO. *SOLID STATE COMMUNICATIONS*, 105:399–402, 1998.

[8] LN Demianets, DV Kostomarov, IP Kuzmina, and SV Pushko. Mechanism of growth of ZnO single crystals from hydrothermal alkali solutions. *Crystallography Reports*, 47:86–98, 2002.

[9] K Bädeker. Über die elektrische Leitfähigkeit und die thermoelektrische Kraft einiger Schwermetallverbindungen. *Annalen der Physik*, 327(4):749–766, 1906.

[10] A Thelen and H König. Elektrische Leitfähigkeit und Struktur aufgestäubter Indiumoxydschichten. *Naturwissenschaften*, 43(13):297–298, 1956.

[11] R Groth and E Kauer. *Philips Technical Review*, 26:105, 1965.

[12] Keith J Laidler, John H Meiser, and Bryan C Sanctuary. *Physical Chemistry*. Houghton Miffin, 2003.

[13] K Ellmer, A Klein, and B Rech. *Transparent Conductive Zinc Oxide, and references therein*. Springer, 2008.

[14] Ü Özgür, YI Alivov, C Liu, A Teke, MA Reshchikov, S Doğan, V Avrutin, SJ Cho, and H Morkoç. A comprehensive review of ZnO materials and devices. *Journal of Applied Physics*, 98:041301, 2005.

[15] B Rech and H Wagner. Potential of amorphous silicon for solar cells. *Applied Physics A: Materials Science & Processing*, 69(2):155–167, 1999.

[16] K Ramanathan, MA Contreras, CL Perkins, S Asher, FS Hasoon, J Keane, D Young, M Romero, W Metzger, R Noufi, et al. Properties of 192% efficiency ZnO/CdS/CuInGaSe 2 thin-film solar cells. *Progress in Photovoltaics: Research and Applications*, 11(4):225–230, 2003.

[17] AD Compaan, A Gupta, S Lee, S Wang, and J Drayton. High efficiency, magnetron sputtered CdS/CdTe solar cells. *Solar Energy*, 77(6):815–822, 2004.

[18] J Nelson. Organic photovoltaic films. *Current Opinion in Solid State & Materials Science*, 6(1):87–95, 2002.

[19] B Szyszka, V Sittinger, X Jiang, RJ Hong, W Werner, A Pflug, M Ruske, and A Lopp. Transparent and conductive ZnO: Al films deposited by large area reactive magnetron sputtering. *Thin Solid Films*, 442(1-2):179–183, 2003.

[20] M Matsuoka. Nonohmic Properties of Zinc Oxide Ceramics. *Japanese Journal of Applied Physics*, 10(6):736–746, 1971.

[21] AR Hutson. Piezoelectricity and Conductivity in ZnO and CdS. *Physical Review Letters*, 4(10):505–507, 1960.

[22] FS Hickernell. Zinc-oxide thin-film surface-wave transducers. *Proceedings of the IEEE*, 64(5):631–635, 1976.

[23] Ruppel, Clemens, and Fjeldly. *Advances in Surface Acoustic Wave Technology, Systems and Applications*. World Scientific Publishing Company, 2000.

[24] K Nomura, H Ohta, A Takagi, T Kamiya, M Hirano, and H Hosono. Room-temperature fabrication of transparent flexible thin-film transistors using amorphous oxide semiconductors. *Nature*, 432(7016):488–492, 2004.

[25] G Thomas. Materials science: Invisible circuits. *Nature*, 389(6654):907, 1997.

[26] K Ando, H Saito, Z Jin, T Fukumura, M Kawasaki, Y Matsumoto, and H Koinuma. Magneto-optical properties of ZnO-based diluted magnetic semiconductors. *Journal of Applied Physics*, 89:7284, 2001.

[27] Z Jin, T Fukumura, M Kawasaki, K Ando, H Saito, T Sekiguchi, YZ Yoo, M Murakami, Y Matsumoto, T Hasegawa, et al. High throughput fabrication of transition-metal-doped epitaxial ZnO thin films: A series of oxide-diluted magnetic semiconductors and their properties. *Applied Physics Letters*, 78:3824, 2001.

[28] S Parkin, X Jiang, C Kaiser, A Panchula, K Roche, and M Samant. Magnetically engineered spintronic sensors and memory. *Proc IEEE*, 91(5):661–680, 2003.

[29] A Steane. Quantum computing. *Reports on Progress in Physics*, 61(2):117–173, 1998.

[30] DC Reynolds, DC Look, B Jogai, CW Litton, G Cantwell, and WC Harsch. Valence-band ordering in ZnO. *Physical Review B*, 60(4):2340–2344, 1999.

[31] H Kim, JS Horwitz, WH Kim, AJ Mäkinen, ZH Kafafi, and DB Chrisey. Doped ZnO thin films as anode materials for organic light-emitting diodes. *Thin Solid Films*, 420:539–543, 2002.

[32] DM Bagnall, YF Chen, Z Zhu, T Yao, S Koyama, MY Shen, and T Goto. Optically pumped lasing of ZnO at room temperature. *Applied Physics Letters*, 70:2230, 1997.

[33] P Zu. Ultraviolet spontaneous and stimulated emissions from ZnO microcrystallite thin films at room temperature. *Solid State Communications*, 103:459–463, August 1997.

[34] K Nomura, H Ohta, K Ueda, T Kamiya, M Hirano, and H Hosono. Thin-Film Transistor Fabricated in Single-Crystalline Transparent Oxide Semiconductor. *Science*, 300(5623):1269, 2003.

[35] N Lowe, N Shaath, and M Pathak. *Sunscreens: Development, Evaluation, and Regulatory*. Marcel Dekker; 2 Rev Sub edition, 1997.

[36] CH Seager and SM Myers. Quantitative comparisons of dissolved hydrogen density and the electrical and optical properties of ZnO. *Journal of Applied Physics*, 94:2888, 2003.

[37] T M Børseth. *Annealing of Ion-implanted and As-Grown Zinc oxide*. PhD thesis, University of Oslo, 2007.

[38] G Heiland, E Mollwo, F Stockman, and F Seitz. Solid State Physics. *New York*, 8:193–323, 1959.

[39] A Janotti and CG Van de Walle. Native point defects in ZnO. *Physical Review B*, 76(16):165202, 2007.

[40] K Wasa, S Hayakawa, and T Hada. Electrical and Optical Properties of Sputtered n-p ZnO-Si Heterojunctions. *Japanese Journal of Applied Physics*, 10:1732–1732, 1971.

[41] KL Chopra. S, Major and DK Pandya. *Thin Solid Films*, 102(1), 1983.

[42] T Minami, H Sato, H Nanto, and S Takata. Group III Impurity Doped Zinc Oxide Thin Films Prepared by RF Magnetron Sputtering. *Japanese Journal of Applied Physics*, 24:L781–L784, 1985.

[43] T Minami, H Sato, H Nanto, and S Takata. Highly conductive and transparent silicon doped zinc oxide thin films prepared by RF magnetron sputtering. *Japanese Journal of Applied Physics*, 25(9), 1986.

[44] J HU and RG GORDON. Textured fluorine-doped ZnO films by atmospheric pressure chemical vapor deposition and their use in amorphous silicon solar cells. *Solar cells*, 30(1-4):437–450, 1991.

[45] T Minami, T Yamamoto, and T Miyata. Highly transparent and conductive rare earth-doped ZnO thin films prepared by magnetron sputtering. *Thin Solid Films*, 366(1-2):63–68, 2000.

[46] JJ Lander. Reactions of Lithium as a Donor and an Acceptor in ZnO. *Journal of Physics and Chemistry of Solids*, 15(2):324–34, 1960.

[47] EC Lee and KJ Chang. Possible p-type doping with group-I elements in ZnO. *Physical Review B*, 70(11):115210, 2004.

[48] MG Wardle, JP Goss, and PR Briddon. Theory of Li in ZnO: A limitation for Li-based p-type doping. *Physical Review B*, 71(15):155205, 2005.

[49] DC Look, DC Reynolds, CW Litton, RL Jones, DB Eason, and G Cantwell. Characterization of homoepitaxial p-type ZnO grown by molecular beam epitaxy. *Applied Physics Letters*, 81:1830, 2002.

[50] CH Park, SB Zhang, and SH Wei. Origin of p-type doping difficulty in ZnO: The impurity perspective. *Physical Review B*, 66(7):73202, 2002.

[51] U Wahl, E Rita, JG Correia, AC Marques, E Alves, and JC Soares. Direct Evidence for As as a Zn-Site Impurity in ZnO. *Physical Review Letters*, 95(21):215503, 2005.

[52] J Carrasco, N Lopez, and F Illas. First Principles Analysis of the Stability and Diffusion of Oxygen Vacancies in Metal Oxides. *Physical Review Letters*, 93(22):225502, 2004.

[53] WE Carlos, ER Glaser, and DC Look. Magnetic resonance studies of ZnO. *Physica B: Physics of Condensed Matter*, 308:976–979, 2001.

[54] YR Ryu, TS Lee, JH Leem, and HW White. Fabrication of homostructural ZnO p–n junctions and ohmic contacts to arsenic-doped p-type ZnO. *Applied Physics Letters*, 83:4032, 2003.

[55] P Fons, H Tampo, AV Kolobov, M Ohkubo, S Niki, J Tominaga, R Carboni, F Boscherini, and S Friedrich. Direct Observation of Nitrogen Location in Molecular Beam Epitaxy Grown Nitrogen-Doped ZnO. *Physical Review Letters*, 96(4):45504, 2006.

[56] Y Yan, SB Zhang, and ST Pantelides. Control of Doping by Impurity Chemical Potentials: Predictions for p-Type ZnO. *Physical Review Letters*, 86(25):5723–5726, 2001.

[57] B Claflin, DC Look, SJ Park, and G Cantwell. Persistent n-type photoconductivity in p-type ZnO. *Journal of Crystal Growth*, 287(1):16–22, 2006.

[58] CG Van de Walle. Hydrogen as a Cause of Doping in Zinc Oxide. *Physical Review Letters*, 85(5):1012–1015, 2000.

[59] CG Van de Walle. Hydrogen as a shallow center in semiconductors and oxides. *physica status solidi (b)*, 235(1):89–95, 2003.

[60] E Mollwo. Die Wirkung von Wasserstoff auf die Leitfähigkeit und Lumineszenz von Zinkoxydkristallen. *Zeitschrift für Physik A Hadrons and Nuclei*, 138:478–488, 1954.

[61] AR Hutson. Hall Effect Studies of Doped Zinc Oxide Single Crystals. *Physical Review*, 108(2):222–230, 1957.

[62] DM Hofmann, A Hofstaetter, F Leiter, H Zhou, F Henecker, BK Meyer, SB Orlinskii, J Schmidt, and PG Baranov. Hydrogen:

A Relevant Shallow Donor in Zinc Oxide. *Physical Review Letters*, 88(4):45504, 2002.

[63] N H Nickel. Influence of the Hydrogen Concentration on H Bonding in Zinc Oxide. *Zinc Oxide - A Material for Micro-and Optoelectronic Applications*, 2005.

[64] XB Li, S Limpijumnong, WQ Tian, HB Sun, and SB Zhang. Hydrogen in ZnO revisited: Bond center versus antibonding site. *Physical Review B*, 78(11), 2008.

[65] K Ip, ME Overberg, YW Heo, DP Norton, SJ Pearton, CE Stutz, B Luo, F Ren, DC Look, and JM Zavada. Hydrogen incorporation and diffusivity in plasma-exposed bulk ZnO. *Applied Physics Letters*, 82:385, 2003.

[66] DC Look, DC Reynolds, JW Hemsky, RL Jones, and JR Sizelove. Production and annealing of electron irradiation damage in ZnO. *Applied Physics Letters*, 75:811, 1999.

[67] DC Look, JW Hemsky, and JR Sizelove. Residual Native Shallow Donor in ZnO. *Physical Review Letters*, 82(12):2552–2555, 1999.

[68] DC Look. Recent advances in ZnO materials and devices. *Materials Science & Engineering B*, 80(1-3):383–387, 2001.

[69] H Shibata, M Watanabe, M Sakai, K Oka, P Fons, K Iwata, A Yamada, K Matsubara, K Sakurai, H Tampo, et al. Characterization of ZnO crystals by photoluminescence spectroscopy. *physica status solidi (c)*, 1(4):872–875, 2004.

[70] RC Newman. *Infrared Studies of Crystal Defects*. Taylor and Francis, London, 1973.

[71] DJ Griffiths. *Introduction to Quantum Mechanics*. Prentice Hall: Upper Saddle River, NJ, 2005.

[72] PM Morse. Diatomic Molecules According to the Wave Mechanics II Vibrational Levels. *Physical Review*, 34(1):57–64, 1929.

[73] C Kittel. *Introduction to Solid State Physics (eight ed)*. John Wiley & Sons, Chichester, 2004.

[74] HD Young and RA Freedman. *Sears and Zemanskys University Physics with Modern Physics*. Addison-Wesley, 2004.

[75] DR Lide. *CRC handbook of chemistry and physics: A Ready-Reference Book of Chemical and Physical Data*. CRC Press, 2004.

[76] SFJ Cox, EA Davis, SP Cottrell, PJC King, JS Lord, JM Gil, HV Alberto, RC Vilão, J Piroto Duarte, N Ayres de Campos, et al. Experimental Confirmation of the Predicted Shallow Donor Hydrogen State in Zinc Oxide. *Physical Review Letters*, 86(12):2601–2604, 2001.

[77] G Müller. *Elektrische und optische Störstellenspektroskopie an ZnO-Kristallen*. PhD thesis, Institut für Angewandte Physik der Universität Erlangen/Nürnberg, 1974.

[78] FG Gartner and E Mollwo. IR absorption of OH and OD centres and OH/OH, OD/OD and OH/OD complexes in Cu-Doped ZnO single crystals. *Physica Status Solidi (b)*, 89:381–388, 1978.

[79] FG Gartner and E Mollwo. IR absorption of OH and OD centres and OH/OH, OD/OD and OH/OD complexes in Cu-Doped ZnO single crystals. *Physica Status Solidi (b)*, 90:33–44, 1978.

[80] MD McCluskey, SJ Jokela, KK Zhuravlev, PJ Simpson, and KG Lynn. Infrared spectroscopy of hydrogen in ZnO. *Applied Physics Letters*, 81:3807, 2002.

[81] G Herzberg. *Molecular Spectra and Molecular Structure I: Spectra of Diatomic Moleclues*. Krieger, Malabar, FL, 1989.

[82] W Ulrici et al. Local-Vibrational-Mode Absorption of Two O$\pm$H Centres in GaP. *Physica Status Solidi (b)*, 210:551, 1998.

[83] EV Lavrov, J Weber, F Börrnert, CG Van de Walle, and R Helbig. Hydrogen-related defects in ZnO studied by infrared absorption spectroscopy. *Physical Review B*, 66(16):165205, 2002.

[84] EV Lavrov, F Börrnert, and J Weber. Dominant hydrogen-oxygen complex in hydrothermally grown ZnO. *Physical Review B*, 71(3):35205, 2005.

[85] EV Lavrov. Infrared absorption spectroscopy of hydrogen-related defects in ZnO. *Physica B: Physics of Condensed Matter*, 340:195–200, 2003.

[86] LE Halliburton, L Wang, L Bai, NY Garces, NC Giles, MJ Callahan, and B Wang. Infrared absorption from OH ions adjacent to lithium acceptors in hydrothermally grown ZnO. *Journal of Applied Physics*, 96:7168, 2004.

[87] GA Shi, M Stavola, and WB Fowler. Identification of an OH-Li center in ZnO: Infrared absorption spectroscopy and density functional theory. *Physical Review B*, 73(8):81201, 2006.

[88] URL: www.spcgoodwill.com, 2008.

[89] T Maqsood. Hydrothermal ZnO; Mastering of Lithium content and formation of Palladium Schottky diodes. Master's thesis, University of Oslo (UiO), Norway, 2008.

[90] M Yamashita and M Agu. Geometrical correction factor for semiconductor resistivity measurements by four-point probe method. *JAP J APPL PHYS*, 23(11):1499–1504, 1984.

[91] LB Valdes. Resistivity Measurements on Germanium for Transistors. *Proceedings of the IRE*, 42(2):420–427, 1954.

[92] BG Streetman. *Solid state electronic devices*. 2006.

[93] SA Campbell. *The science and engineering of microelectronic fabrication*. Oxford University Press New York, 2001.

[94] PR Griffiths and JA De Haseth. *Fourier Transform Infrared Spectroscopy*. John Wiley & Sons, 2007.

[95] WL Bond. Measurement of the Refractive Indices of Several Crystals. *Journal of Applied Physics*, 36:1674, 1965.

[96] GH Aylward and TJV Findlay. *SI Chemical Data*. Wiley, 2002.

[97] RJ Bell. *Introduction Fourier Transform Spectroscopy*. Academic Press, 1972.

[98] Brukeroptics. Reference manual OPUS. *BRUKER OPTIK*, 2, 2004.

[99] P Fellgett. Theory of multiplex interferometric spectrometry. *Journal de Physique et Le Radium*, 19:187–191, 1958.

[100] P Jacquinot. New developments in interference spectroscopy. *Reports on Progress in Physics*, 23(1):267–312, 1960.

[101] PR Griffiths and C Homes. *Instrumentation for Far-infrared Spectroscopy*. Brookhaven National Laboratory, Upton, NY (US), 2001.

[102] RJ Collins and DA Kleinman. Infrared Reflectivity of Zinc Oxide. *Journal of Physics and Chemistry of Solids*, 11:190–194, 1959.

[103] NK Morozova, VG Plotnichenko, EM Gavrishchuk, and VV Blinov. Absorption Spectrum of ZnO Precipitates in ZnSe. *Inorganic Materials*, 39(8):783–787, 2003.

[104] PY Emelie, JD Phillips, B Buller, and UD Venkateswaran. Free carrier absorption and lattice vibrational modes in bulk ZnO. *Journal of Electronic Materials*, 35(4):525–529, 2006.

[105] E Ruiz, S Alvarez, and P Alemany. Electronic structure and properties of AlN. *Physical Review B*, 49(11):7115–7123, 1994.

[106] KM Johansen, JS Christensen, EV Monakhov, AY Kuznetsov, and BG Svensson. Deuterium diffusion and trapping in hydrothermally grown single crystalline ZnO. *Applied Physics Letters*, 93:152109, 2008.

[107] URL: www.srim.org, 2008.

[108] JF Ziegler, JP Biersack, and MD Ziegler. *SRIM-The Stopping and Range of Ions in Matter*. SRIM Co, 2008.

[109] R Schifano, EV Monakhov, L Vines, and BG Svensson. Role of Lithium and Aluminium on the electrical properties of hydrothermally grown n-type ZnO. *To be published*.

[110] JC Owrutsky, NH Rosenbaum, LM Tack, and RJ Saykally. The vibration-rotation spectrum of the hydroxide anion (OH). *The Journal of Chemical Physics*, 83:5338, 1985.

[111] GA Shi, M Saboktakin, M Stavola, and SJ Pearton. "Hidden hydrogen" in as-grown ZnO. *Applied Physics Letters*, 85:5601, 2004.

[112] SZ Karazhanov and AG Ulyashin. Role of diatomic hydrogen in the electronic structure of ZnO. *Physical Review B*, 78(8), 2008.

[113] F Tuomisto, K Saarinen, DC Look, and GC Farlow. Introduction and recovery of point defects in electron-irradiated ZnO. *Physical Review B*, 72(8):85206, 2005.

[114] YV Gorelkinskii and GD Watkins. Defects produced in ZnO by 25-MeV electron irradiation at 42 K: Study by optical detection of electron paramagnetic resonance. *Physical Review B*, 69(11):115212, 2004.

[115] LS Vlasenko and GD Watkins. Optical detection of electron paramagnetic resonance in room-temperature electron-irradiated ZnO. *Physical Review B*, 71(12):125210, 2005.

[116] P Erhart and K Albe. Diffusion of zinc vacancies and interstitials in zinc oxide. *Applied Physics Letters*, 88:201918, 2006.

[117] P Erhart and K Albe. First-principles study of migration mechanisms and diffusion of oxygen in zinc oxide. *Physical Review B*, 73(11):115207, 2006.

[118] C Coskun, DC Look, GC Farlow, and JR Sizelove. Radiation hardness of ZnO at low temperatures. *Semiconductor Science and Technology*, 19(6):752–754, 2004.

[119] S Klauer, M Wöhlecke, and S Kapphan. Influence of HD isotopic substitution on the protonic conductivity of $LiNbO_3$. *Physical Review B*, 45(6):2786–2799, 1992.

[120] JB Bates and RA Perkins. Infrared spectral properties of hydrogen, deuterium, and tritium in TiO_2. *Physical Review B*, 16(8):3713–3722, 1977.

[121] R González, R Pareja, and Y Chen. Protons in neutron-irradiated and thermochemically reduced MgO crystals doped with lithium impurities. *Physical Review B*, 45(22):12730–12735, 1992.

[122] R González, I Vergara, D Cáceres, and Y Chen. Role of hydrogen and lithium impurities in radiation damage in neutron-irradiated MgO single crystals. *Physical Review B*, 65(22):224108, 2002.

[123] MK Linnarsson, MS Janson, S. Karlsson, A. Schöner, N. Nordell, and BG Svensson. Diffusion of light elements in 4H–and 6H–SiC. *Materials Science & Engineering B*, 61:275–280, 1999.

[124] S Limpijumnong and SB Zhang. Resolving hydrogen binding sites by pressure - A first-principles prediction for ZnO. *Applied Physics Letters*, 86:151910, 2005.

[125] M Sano, H Kato, et al. Method of manufacturing ZnO substrate from ZnO crystal formed by hydrothermal synthesis method, March 29 2006. US Patent App 11/392,863.